Research Article | Open Access

Microstructures

Rabbitt *et al. Microstructures* **2026**, *6*, 20260112 **DOI:**10.20517/microstructures.2026.101

Amplifying the antimicrobial efficacy of titanium-copper alloys through blended powder laser powder bed fusion

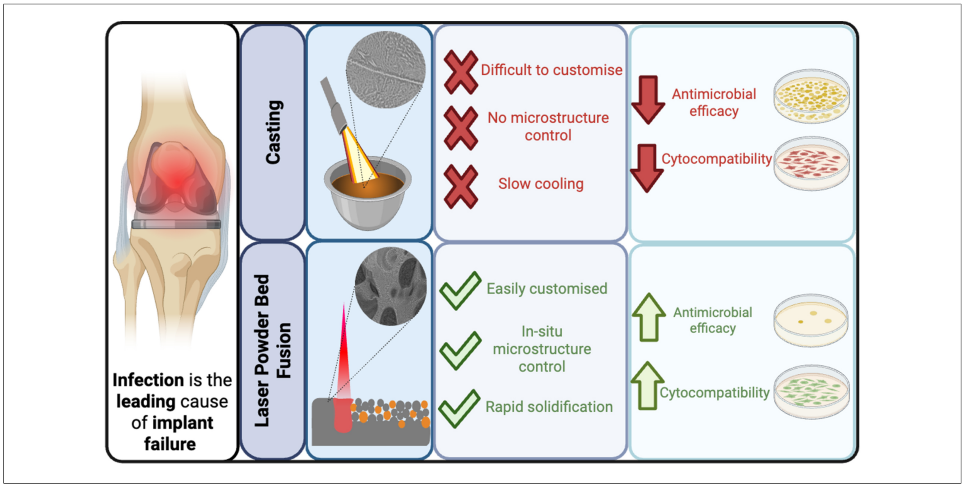
Daisy Rabbitt[1], Kevin Couling[2], Lichen Guan[3], René Daniel Pütz[3], Saman Nikpour[3], Victor M. Villapún[4], Luke N. Carter[1], Greg Gibbons[2], Richard Hague[5], Jonathan Stevenson[1,6], Yolanda Hedberg[3,7], Alexander J. Knowles[8], Sophie C. Cox[1]

Keywords:
Additive manufacturing, microstructure, corrosion, ion release, infection

Citation: Rabbitt, D.; Couling, K.; Guan, L.; Pütz, R. D.; Nikpour, S.; Villapún, V. M.; Carter, L. N.; Gibbons, G.; Hague, R.; Stevenson, J.; Hedberg, Y.; Knowles, A. J.; Cox, S. C. Amplifying the antimicrobial efficacy of titanium-copper alloys through blended powder laser powder bed fusion. *Microstructures* **2026**, *6*, 20260112. https://dx.doi.org/10.20517/microstructures.2026.101

Received: 11 May 2026
First Decision: 18 Jun 2026
Revised: 30 Jun 2026
Accepted: 17 Jul 2026
Published: 27 Aug 2026

Academic Editor:
Huijun Li
Copy Editor:
Fangling Lan
Production Editor:
Fangling Lan



Abstract

Skeletal implant infection (peri-implantitis) remains a major clinical challenge, despite identification of alloy compositions with promising antimicrobial performance. This study explores the opportunity to refine the microstructure of alloys through blended powder laser powder bed fusion (BP-LPBF) manufacturing, focusing on enhancing biological responses. Using antimicrobial Ti-Cu alloys as a case study system, we show that BP-LPBF produces distinct microstructures compared to conventional casting, with performance governed by the spatial distribution and connectivity of Cu-rich phases rather than composition alone. Ti-3Cu (wt%) was found to achieve a refined microstructure with minimal intermetallic formation, strong antibacterial performance (> 99% *S. aureus* and *E. coli* after 24 h), and excellent cytocompatibility (78% after 7 days). In contrast, Ti-11.5Cu exhibited superior antibacterial effects (99.9% for *S. aureus* and 99.99% for *E. coli*) due to higher Cu ion release, microstructural heterogeneity, and greater Ti_2Cu formation; however*

[1]School of Chemical Engineering, University of Birmingham, Birmingham B15 2TT, UK.
[2]Warwick Manufacturing Group (WMG), University of Warwick, Coventry CV4 7AL, UK.
[3]Department of Chemistry, The University of Western Ontario, London, ON N6A 5B7, Canada.
[4]School of Mechanical Engineering, University of Birmingham, Birmingham B15 2TT, UK.
[5]Centre for Additive Manufacturing, Faculty of Engineering, University of Nottingham, Nottingham NG8 1BB, UK.
[6]Royal Orthopedic Hospital, Birmingham B31 2AP, UK.
[7]Surface Science Western, The University of Western Ontario, London, ON N6G 0J3, Canada.
[8]School of Metallurgy and Materials, University of Birmingham, Birmingham B15 2TT, UK.

Correspondence to: Dr. Sophie C. Cox, School of Chemical Engineering, University of Birmingham, Birmingham B15 2TT, UK. E-mail: s.c.cox@bham.ac.uk

it suffered from compromised ductility and cytotoxicity. Importantly, Cu ion release from all alloys was several orders of magnitude lower than reported bactericidal thresholds, indicating that antimicrobial activity is predominantly governed by surface-mediated mechanisms rather than bulk ion release. Spatially localised Cu-rich phases generate micro-galvanic interactions and potentially elevated near-surface Cu activity, enabling effective bacterial inactivation. Under oxidative conditions, increased ion release provides a secondary contribution, supporting a dual-mechanism model. Compared to cast equivalents, BP-LPBF fabricated Ti-Cu alloys exhibited enhanced bio-functionality even at lower Cu levels. Beyond acting as a powerful platform for accelerating alloy development, we also demonstrate LPBF production of multi-material implants with antimicrobial Ti-Cu surface features.

INTRODUCTION

To date, manufacture of biomedical titanium alloys has traditionally been achieved by conventional methods, including arc melting, ball milling and sintering, or forging[1-8]. Whilst these methods are widely employed at industrial scales, for alloy discovery the iterative nature and reliance on post-manufacturing processing (e.g., heat treatments) hinder rapid screening. In contrast, additive manufacturing (AM), and particularly laser powder bed fusion (LPBF), offers a paradigm shift in alloy design and optimisation, providing a platform that enables rapid, cost-effective exploration of novel material systems[9]. Through the *in situ* alloying of blended elemental powders, LPBF alloys enable direct fabrication of customised compositions, circumventing the need for traditional melting and casting. This flexibility is especially advantageous in the early stages of alloy discovery when there may be a high degree of compositional uncertainty and refining the target zone may be the priority. When considering the incorporation of particularly expensive rare elements, e.g., Ag and Ta to drive beneficial biological functions, this rapid 'zoning in' principle along small-scale exploration is especially favourable[10-13].

LPBF has already proven effective in fabricating dense, complex medical device components, in particular for Ti-based alloys[14-19]. Alongside production machines, several alloy development platforms have also entered the metal AM space in recent years, indicating the potential for LPBF to also be used for materials discovery. Such systems or utilisation of reduced build volumes (RBV) allow users to rapidly screen multiple alloy variants using relatively small quantities of raw material. This high-throughput alloy discovery potential may be particularly valuable for systems where composition-microstructure-property relationships are intricate and non-linear, as found in antimicrobial Ti-Cu alloys[20,21]. Biomedical applications, in particular, benefit from this agility as alloy candidates must satisfy dual demands of mechanical reliability and biological performance, such as biocompatibility and osseointegration. A similar need for balance is observed in other fields such as aerospace, where high-temperature turbine blade alloys must optimize two key performance metrics: operating temperature and specific strength[22].

Beyond compositional variation, microstructural control is equally critical for determining the mechanical performance of components. Microstructural features have also been shown to significantly influence biological performance[23-25]. The rapid cooling rates and steep thermal gradients inherent to LPBF (typically 10^3-10^6 K/s) specifically offer the opportunity to form non-equilibrium microstructures, such as supersaturated solid solutions and refined grains, which can have a profound impact on both mechanical and biological properties[26-28]. For instance, Thampy *et al.* demonstrated that adjusting laser power directly impacts cooling rate, enabling optimisation of microstructure and control of residual stresses[29]. Moreover, the layer-by-layer nature of LPBF enables spatial control over thermal gradients, allowing for the customisation of microstructural features in three dimensions. In the context of medical device

manufacturing, this opens up the possibility of producing graded components with tailored surface properties to drive specific cellular responses, while preserving mechanical integrity in the bulk material[30,31]. For example, in orthopaedics many devices with lattices at the surface are being produced to facilitate tissue integration. Here, the composition and microstructure of the porous sections could be further tuned to support bone cell adhesion and mineralisation, or to inhibit bacterial growth.

It is particularly notable that LPBF offers many in-process opportunities to tailor microstructure, which is in contrast to conventional metal-forming processes that typically rely on post-processing heat treatments[20,21]. Specifically, LPBF microstructure control may be achieved during fabrication via laser parameter modulation[30,32] and scanning strategy design[33,34]. These adaptations may impact elemental segregations, grain size and morphology[35,36], surface topography[37,38], as well as the passive layer stability[39]. These in turn potentially offer further opportunities to tailor the formed alloy. In this context, LPBF provides a unique methodology to couple process design with functional performance, enabling integrated control over structure, composition, and surface properties.

Titanium and its alloys have become the most widely utilised materials for biomedical implants, due to their good mechanical properties, accepted biocompatibility, high corrosion resistance and their ability to enable osseointegration[39,40]. However, despite the advantages of Ti-based implants, these alloy systems lack inherent mechanisms to prevent bacterial adhesion or biofilm formation, which promote prosthetic joint infection (PJI). PJI is the leading cause of early implant failure, resulting in morbid revision surgeries, prolonged hospital admissions, high cost to the health economy, and remains limb-threatening. Engineering antimicrobial surfaces represents a promising approach to mitigating bacterial biofilm formation by preventing initial bacterial adhesion and colonisation. The incorporation of antimicrobial elements, such as Cu, into Ti-alloy systems has been shown to inhibit bacterial attachment and proliferation, thereby reducing the likelihood of biofilm development[41].

Given the increasing demand for multifunctional biomedical alloys, titanium-copper (Ti-Cu) systems have emerged as strong candidates due to their high antimicrobial potential. The ability of LPBF to rapidly fabricate and evaluate compositional variants makes it especially suited to optimise these alloys. Nevertheless, integrating Cu via LPBF is not without challenges. Copper's high reflectivity (up to 98% of a 1,000-1,100 nm laser) presents difficulties in laser absorption and melt pool stability, requiring careful parameter optimisation[42-45]. Moreover, LPBF components often exhibit defects such as porosity and high surface roughness, which may necessitate post-processing to ensure mechanical and biological performance[43]. Therefore, Cu content optimisation is necessary to balance the antimicrobial efficacy of the material, as well as the manufacturability and mechanical properties.

Driven by the clinical need for advanced biomaterials with enhanced antimicrobial performance, this study investigates the development of next-generation Ti-Cu alloys using blended powder laser powder bed fusion (BP-LPBF). Herein, we explore opportunities to enable precise microstructural tuning, resulting in functional advantages over conventional cast counterparts. This study highlights the opportunities that BP-LPBF offers for alloy microstructural tuning, demonstrating that these benefits can be significant for biomedical components.

METHODS

Target compositions

Ti-3Cu alloys have previously been reported to exhibit antimicrobial activity[1,46-50], although previously researched ĕħ cast Ti-11.5Cu alloys were deemed to have no efficacy[20]. In this study, Ti-3Cu and Ti-11.5Cu (wt%) were selected due to their ability to produce different phases and microstructures according to the

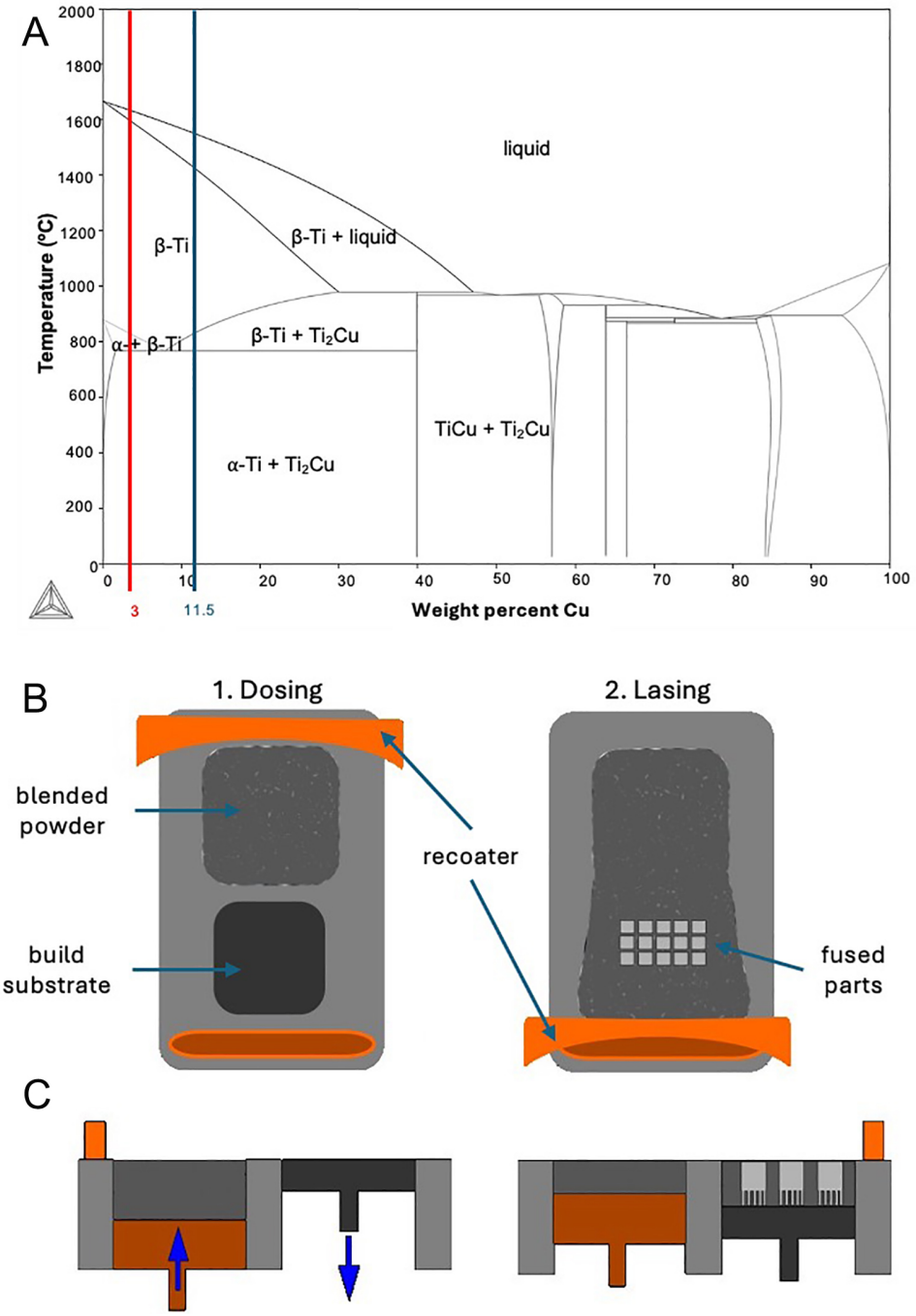


Figure 1. (A) Binary Ti-Cu phase diagram generated using Thermo-Calc 2023a and the TCTI2 database. The red and blue lines represent the Ti-3Cu and Ti-11.5Cu alloy compositions investigated in this work. (B and C) manufacturing process of blended powder samples through the use of a reduced build volume (RBV) unit.

phase diagram [Figure 1], and to investigate the use of BP-LPBF on the antimicrobial efficacy of these alloys.

Casting of Ti-Cu alloys

Ti-11.5Cu ingots were produced using an Arcast Arc200 arc melter (Alloyed Ltd). Pure titanium sponge and solid pure copper (grade C101) were used. Melting was conducted in a copper crucible equipped with a tilt-casting arrangement and copper mould. To promote compositional uniformity within the melt, electromagnetic stirring was applied throughout processing. Prior to melting, the chamber was evacuated to

approximately 10^{-2} bar and subsequently backfilled with high-purity argon to provide an inert atmosphere during alloy fabrication.

Production of Ti-Cu alloys via BP-LPBF

Blended powder feedstocks were prepared from commercially pure (grade 1) titanium (AP&C, Boisbriand, Canada) and high-purity OFHC copper (Eckart, TLS GmbH, Bitterfeld-Wolfen, Germany) powders. The titanium and copper powders exhibited particle size distributions of 15-45 and 15-53 μm, respectively. Mixtures corresponding to Ti-3Cu and Ti-11.5Cu (wt.%) compositions were weighed under an Ar atmosphere and homogenised using a roller blender for 8 h.

Particle size distribution was checked using a Malvern Mastersizer 2000 system (Malvern Panalytical, UK) based on laser diffraction analysis, with deionised water employed as the dispersant medium. Powder morphology was characterised using backscattered electron (BSE) imaging on a ZEISS EVO10 (Zeiss, Germany) scanning electron microscope. For imaging, powder particles were mounted onto carbon adhesive tabs and lightly agitated to remove loosely bound excess material prior to analysis.

The blended powders were then subsequently processed into cuboidal specimens measuring 10 × 10 × 10 mm using a LPBF system. Fabrication was carried out on a 500 W 1,070 nm ytterbium fibre laser on a RenAM500S (Renishaw, UK) machine equipped with a RBV unit. All samples were built on Ti-6Al-4V substrates under a controlled argon atmosphere, with oxygen concentrations maintained below 1,000 ppm throughout the laser processing stage.

Parametric studies were initially performed to optimise laser power (100-300 W) and scan speeds (200-1,000 mm/s) to ensure maximum densification of specimens with minimal porosity. Builds were then repeated for each Ti-Cu blend with the optimised parameters to produce specimens for characterisation and *in vitro* testing. Ti-3Cu specimens were processed at 100 W laser power and 400 mm/s effective scan speeds, whereas Ti-11.5Cu specimens were manufactured at lower laser energy density at 100 W laser power and 1,000 mm/s. Ti-6Al-4V controls were also manufactured using 200 W and 1,500 mm/s processing conditions. All other parameters were kept consistent: layer thickness 30 μm, exposure point distance 90 μm, hatch distance 90 μm, spot diameter 75 μm, and layer angle 67°.

After mechanical removal from the build plate, the alloys were then sectioned parallel to the build direction into 10 × 10 × 2 mm coupons for all characterisation and *in vitro* experiments. Samples utilised for electron microscopy were subsequently mounted in conductive Bakelite. All specimens were mechanically ground to 1,200 grit, then polished with diamond and non-activated oxide polishing suspension (OPS) solutions.

The cubes were cut parallel to the building direction into 10 × 10 × 1 mm coupons using electrical discharge machining (EDM) with filtered water as a coolant for metal release immersion tests described in section "Ti and Cu ion release". For immersion tests, one of the coupons' 10 × 10 mm surfaces was stepwise ground to P2500. All coupons for immersion tests were ultrasonically cleaned in acetone and ethanol for 5 min each, rinsed with ultrapure water (18.2 MΩ·cm resistivity) from a Milli-Q Reference System (Millipore Sigma, USA), and dried with Ar gas after the final grinding/polishing step. The immersion test coupons were stored in a desiccator with low humidity for at least 24 h prior to the experiment to allow reproducible surface oxide formation. Any non-ground surfaces (back side and edges) were sealed with a metal-free acrylic lacquer nail polish (acrylate), exposing a surface area of 1 cm^2 to the solutions.

Microstructural characterisation and phase identification

Scanning electron microscopy (SEM) was carried out to observe alloy microstructure (ZEISS EVO10, Germany), using a backscattered electron detector to reveal compositional contrast. Phase identification through X-Ray Diffraction (XRD) was performed in an AXRD system (Proto Manufacturing Inc, Tayor, USA) equipped with a copper line focus X-ray tube, a nickel k_β absorber producing K_α radiation ($K_{\alpha_{av}}$ = 1.541874 Å), a set increment size of 0.0149282° and a power setting of 30.0 kV and 20 mA.

Backscatter electron SEM images of Ti-3Cu AM and Ti-11.5Cu AM were analysed to quantify microstructural heterogeneity based on greyscale intensity variations. Images were converted to greyscale and normalised to a [0, 1] intensity range. All analysis was performed in MATLAB (MathWorks, USA). Greyscale intensity distributions were obtained using 256-bin histograms. Global heterogeneity was quantified using the mean greyscale intensity (μ), standard deviation (σ), coefficient of variation (CV = σ/μ), and entropy, calculated from the intensity probability distribution using Shannon's definition[51,52]. Spatial heterogeneity was assessed using local standard deviation mapping, computed with a 15 × 15 pixel moving window (stdfilt). This produced maps of local intensity variation (σ_local), highlighting regions of increased microstructural contrast. For comparison, all heterogeneity maps were displayed using a common colour scale based on the global minimum and maximum σ_local values.

Ti and Cu ion release

The solutions were prepared using phosphate-buffered saline (PBS), which contained 8.77 g/L NaCl, 1.28 g/L Na_2HPO_4, and 1.36 g/L KH_2PO_4 (all ≥ 99%, Fisher Scientific), bovine serum albumin (BSA, heat shock fraction, pH 7, ≥ 98%, Sigma-Aldrich (A7906), USA), NaOH (ACS grade, Fisher Scientific, USA), 30% w/w H_2O_2 (ACS grade, Fisher Scientific, USA), and ultra-pure water. Two solutions were prepared to simulate benign and harsh (inflamed) conditions[53], respectively: PBS and PBS + 10 g/L BSA + 30 mM H_2O_2. The pH of both solutions was adjusted to approximately 7.3 by adding 350 μL/L of 8 M NaOH solution.

The coupons with 1 cm^2 exposed surface area were immersed in 5 mL of the test solutions. The samples were placed in a dark incubator at 37 °C with gentle rotational agitation of 80 rpm for 24 h. The metal release analysis was conducted in triplicate with a minimum of three background controls (blanks) for each solution. After 24 h, the specimens were removed from the solution and rinsed with 1 mL of ultrapure water added to the solution. The rinsing ensured the collection of any species loosely attached to the surface. The BSA-containing solution was then frozen before digestion and trace-metal solution analysis.

For digestion, 3 mL of each solution was pipetted into individual tubes. Then, 333 μL of pure ≥ 65% nitric acid (*puriss. p.a.* grade, Sigma-Aldrich (A30709), USA) was added to the 3 mL solutions. Microwave digestion was performed for PBS + 10 g/L BSA + 30 mM H_2O_2 using an Anton Paar Multiwave 7,000 digestion system at 220 °C for 20 min to allow temperature ramping, followed by 10 min holding at 220 °C and 140 bar. After digestion, the final volume was adjusted to 10 mL with ultrapure water.

The amounts of Cu and Ti released into the solutions relative to the blanks were measured using a Thermo Scientific iCAP Q inductively coupled plasma mass spectrometry (ICP-MS) instrument in KED (kinetic energy discrimination) mode using He as collision gas. The instrument was calibrated with eight prepared standards (0, 0.5, 2, 5, 10, 25, 50, and 100 μg/L) of Ti and Cu. The calibration standards were prepared using acidified PBS and microwave-digested PBS for the PBS solution and the PBS + 10 g/L BSA + 30 mM H_2O_2 solution, respectively. Because of the effect of chlorides on plasma temperature, the chloride concentration was maintained constant in all standards and samples. Additionally, an internal Sc standard was used to correct for signal fluctuations. The amount of released metals was calculated using Eq. (1).

$$\text{Amount of released metals } \left(\frac{\mu g}{cm^2}\right) = \frac{\left(c_{Sample}\left(\frac{\mu g}{L}\right) - c_{Blank}\left(\frac{\mu g}{L}\right)\right) \times DF \times 0.005(\ L)}{A(cm^2)} \quad (1)$$

where c_{Sample} and c_{Blank} are the sample concentration and blank concentration, respectively. Each specimen's exposure volume was 0.005 L. All containers and materials in contact with solutions were acid-cleaned in 10% HNO_3 for at least 24 h, then rinsed with ultrapure water and air-dried.

Contact angle analysis

Surface wettability was assessed by contact angle (CA) measurements using the sessile drop method on an Attension Theta Lite Tensiometer (Biolin Scientific, USA). A 5 µL droplet of deionised water was dispensed onto the sample surface, and the CA was recorded after an equilibration period of 5 s. For each specimen, three independent measurements were performed at different locations, and the reported value is the mean CA.

Mechanical testing

Microhardness

Microhardness testing was carried out using a Wilson VH1202 Vickers hardness tester (Buehler, Germany) with a 100 g load and 50× magnification. Five indentations were made on each mounted and polished sample in a quincunx arrangement. Manual adjustments were applied when necessary to correct software-based corner-detection errors. The final hardness value for each specimen was calculated as the mean of the five measurements.

Tensile testing

Ti-Cu builds were carried out to manufacture samples of 20 mm height, 5 mm width, and 1mm thickness. From these specimens, SS-J3 tensile bars (gauge length of 7.63 mm) were cut using a wire-cutting EDM, with geometries as described in Gussev *et al.*, 2014[54]. Tensile testing was conducted at temperatures between 20-22 °C using an Instron 3367 tensile testing machine (Instron, Norwood, USA) equipped with a 10 kN load cell. Testing followed the ASTM E8 standard, with three replicates studied. A video extensometer for strain measurement employing a reduced optics configuration to achieve a 60 mm field of view suitable for small sample sizes was used. The dimensions of each specimen were determined by measurements taken at three points using a micrometer, averaging across 5 sample conditions. Ductility was calculated using percentage elongation up to the breaking point of the specimens.

In vitro testing

Antimicrobial analysis

To evaluate the antibacterial performance of the Ti-Cu alloys, two representative pathogenic strains commonly implicated in PJIs were selected: *Staphylococcus aureus* (Newman strain), a Gram-positive bacterium frequently associated with implant-related infections[55], and *Escherichia coli* (K12), a model Gram-negative organism. Both bacteria were obtained from the Birmingham Dental Hospital. Prior to testing, all samples were sterilised by immersion in pure ethanol under dark conditions for 30 min, followed by drying for 24 h.

Antimicrobial activity was assessed in accordance with ISO 22196:2011 and JIS Z 2801[56]. Each sample was inoculated with a 5 µL bacterial suspension, and a sterile coverslip was placed on top. The specimens were then positioned in Petri dishes containing sterile tissue paper saturated with 2 mL of sterile Dulbecco's phosphate-buffered saline (DPBS) and incubated at 37 °C for 24 h. Following incubation, each coupon was transferred into 5 mL of DPBS and vortexed for 2 min to detach and resuspend the bacteria, ensuring

separation of the coverslip from the sample surface. Subsequently, 100 µL of the resulting suspension was transferred into a 96-well plate and serially diluted ten-fold in DPBS. 10 µL aliquots from each dilution were then spread onto Mueller-Hinton agar plates to ensure uniform bacterial distribution. Plates were incubated at 37 °C for a further 24 h before colony enumeration. Colony-forming units (CFU/mm²) were calculated using the plate count method according to the dilution factor, using the expression: CFU/mm² = (number of colonies × $10^{\text{dilution factor}}$)/100 mm².

Bacterial reduction was calculated using Eq. (2), where N_{Ti64} relates to the colony-forming units per mm², CFU/mm² count for the Ti64 control, whereas N_x represents the CFU for each condition tested.

$$\text{Bacterial reduction } (\%) = \frac{N_{Ti64} - N_x}{N_{Ti64}} \times 100 \quad (2)$$

The percentage bacterial reduction was determined relative to the Ti-6Al-4V control, which was defined as the baseline (0% antibacterial activity).

Mammalian cell analysis

Murine pre-osteoblast MC3T3 cells Subclone 4 (ATCC-CRL-2593), from American Type Culture Collection (ATCC, United Kingdom), were cultured in T75 flasks and incubated at 37 °C in basal media consisting of Dulbecco's Modified Eagle's Medium (DMEM) supplemented with 10% fetal bovine serum, 12% L-glutamine, and 1% penicillin/streptomycin. Once approximately 80% semiconfluency was reached, cells were detached and resuspended for seeding onto the samples at a density of 2 × 10^4 per coupon. After 20 min of initial cell attachment, 1 mL of fresh basal media was added to each well and cells incubated at 37 °C and 5% CO_2.

Cell viability was assessed using a LIVE/DEAD staining assay, performed on three samples per condition. Specimens were incubated with 200 µL of a 5 mM calcein-AM and 1.5 mM propidium iodide solutions for 30 min. After staining, samples were inverted and imaged using an EVOS M5000 microscope (Invitrogen, USA) at 10× magnification. Viability was quantified using ImageJ (version 1.54j)[57] by calculating the proportion of green fluorescent (viable) cells relative to the total cell population.

Metabolic activity and cell proliferation of cells were evaluated using an Alamar Blue assay. A total of 0.75 mL of basal DMEM supplemented with 10% Alamar Blue reagent was added to each sample and incubated for 4 h at 37 °C. Fluorescence measurements were then acquired using a microplate reader (Spark, Tecan Trading AG, Switzerland) at excitation and emission wavelengths of 560 and 590 nm, respectively. All experiments were carried out in triplicate.

Statistical analysis

All statistical analyses were performed using GraphPad Prism (version 9.0.0, GraphPad Software, USA). Data are presented as mean ± standard deviation (SD). Prior to analysis, normality of the data distributions was assessed using the Shapiro-Wilk test, and homogeneity of variance was evaluated using Levene's test.

For CA and antimicrobial activity data, ordinary one-way analysis of variance (ANOVA) was applied to determine statistically significant differences between sample compositions. Where significant effects were identified, post-hoc multiple comparisons were performed using Tukey's test. Statistical significance was defined as $P < 0.05$.

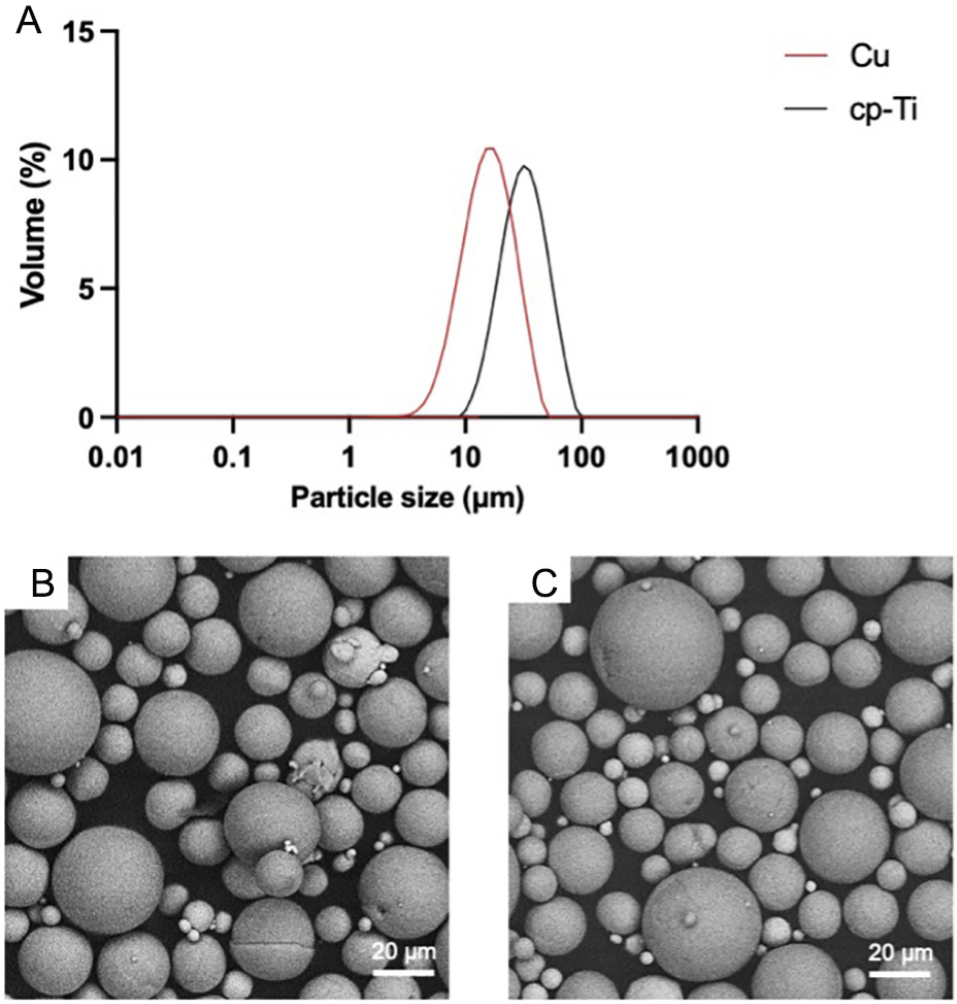


Figure 2. (A) Particle size analysis of cp-Ti and Cu powders and (B) Ti-3Cu and (C) Ti-11.5Cu powder blend SEM micrographs. Particle size analysis of cp-Ti shows a greater particle size and wider range than the Cu powder. Cu powder in images (B and C) appears brighter than Ti powder, This figure is reprinted with permission[21].

For ICP-MS data, comparisons between two independent groups were conducted using an unpaired Student's *t*-test with unequal variances (Welch's correction), performed in KaleidaGraph (version 4.0). In all cases, statistical significance was set at $P < 0.05$.

RESULTS

BP-LPBF parameter optimisation

The particle size distribution analysis in Figure 2A indicates that both cp-Ti and Cu powders exhibit a similar size range. Cu possesses a smaller average particle size (17.5 μm), compared to cp-Ti (35 μm). The Cu powder possesses a D10 of 7.5 μm and D90 of 27 μm, whereas cp-Ti has a D10 of 17 μm and D90 of 50 μm. This indicates that the particle size distribution of Cu powder is narrower and more uniform than that of cp-Ti. The BSE SEM micrographs in Figure 2B and C illustrate the morphology of Ti-Cu powder blends with increasing Cu content. The powders exhibit a generally spherical morphology, which is characteristic of gas-atomised metal powders, with a range of particle sizes that appear to agree with the size range depicted in Figure 2A. In Ti-3Cu [Figure 2B], the particles appear relatively uniform with minimal satellite formation. As the Cu content increases to Ti-11.5Cu [Figure 2C], the presence of finer particles and particle clustering becomes more evident, potentially indicating differences in powder flowability and distribution.

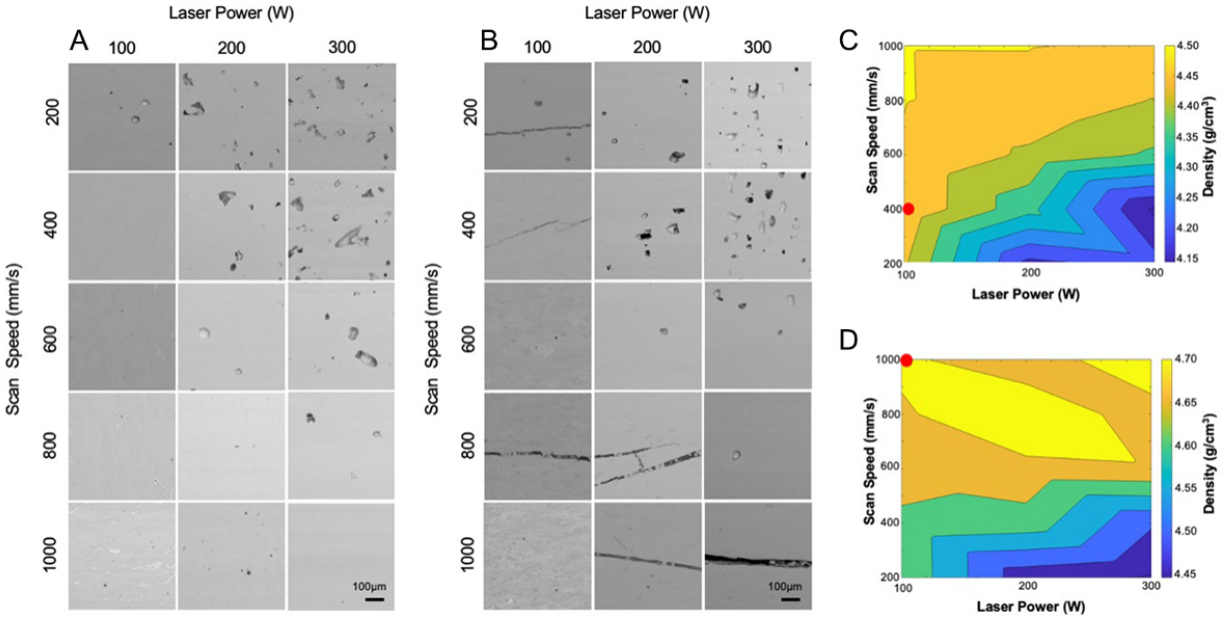


Figure 3. Process parameter optimisation and densification behaviour of BP-LPBF Ti-Cu alloys. (A and B) Representative micrographs of Ti-3Cu (A) and Ti-11.5Cu (B) samples produced across a range of laser powers (100-300 W) and scan speeds (200-1,000 mm/s), illustrating the evolution of porosity and defect morphology with processing conditions. Samples were sectioned parallel to the build direction, and all micrographs are displayed with the build direction oriented vertically upwards. (C and D) Corresponding density contour maps for Ti-3Cu (C) and Ti-11.5Cu (D), showing the compositional dependence of the optimal processing window. Red dots represent the optimal processing conditions for Ti-3Cu (C) and Ti-11.5Cu (D), This figure is reprinted with permission[21].

Parametric studies were conducted to evaluate the influence of laser power (100-300 W) and scan speed (200-1,000 mm/s) on densification and defect formation in Ti-3Cu and Ti-11.5Cu alloys [Figure 3]. Representative microstructures across the processing window [Figure 3A and B] demonstrate a strong dependence of porosity and defect morphology on energy input. At low scan speeds (< 600 mm/s) and high laser powers (> 200 W), increased melt pool instability and keyhole-type porosity were observed, while insufficient energy density at high scan speeds resulted in lack-of-fusion defects and incomplete consolidation. An optimal processing window is therefore required to balance sufficient melting with melt pool stability. Density contour maps [Figure 3C and D] further highlight the compositional dependence of this processing window. Ti-3Cu exhibited a broader region of high relative density, with near-full densification achieved at moderate scan speeds (~400-800 mm/s) and lower laser powers (100 W). In contrast, Ti-11.5Cu showed a narrower optimal processing window and required lower effective energy input to minimise defect formation. At higher energy densities, Ti-11.5Cu displayed increased porosity and microstructural instability, likely associated with enhanced Cu segregation, altered melt pool dynamics, and differences in thermal conductivity and laser absorption behaviour compared to Ti-3Cu.

Based on these observations, optimised parameters were selected to achieve maximum densification with minimal porosity for each composition, as marked by red dots in Figure 3C and D. Ti-3Cu samples were processed at 100 W and 400 mm/s, corresponding to a stable, high-density region within the processing map. In contrast, Ti-11.5Cu required a lower energy density condition of 100 W and 1,000 mm/s to avoid defect formation and maintain structural integrity. These findings demonstrate that Cu content significantly influences processability during BP-LPBF, necessitating composition-specific parameter optimisation. Importantly, this highlights the capability of AM not only to fabricate Ti-Cu alloys, but to actively tailor their microstructure and macrostructure through controlled processing conditions.

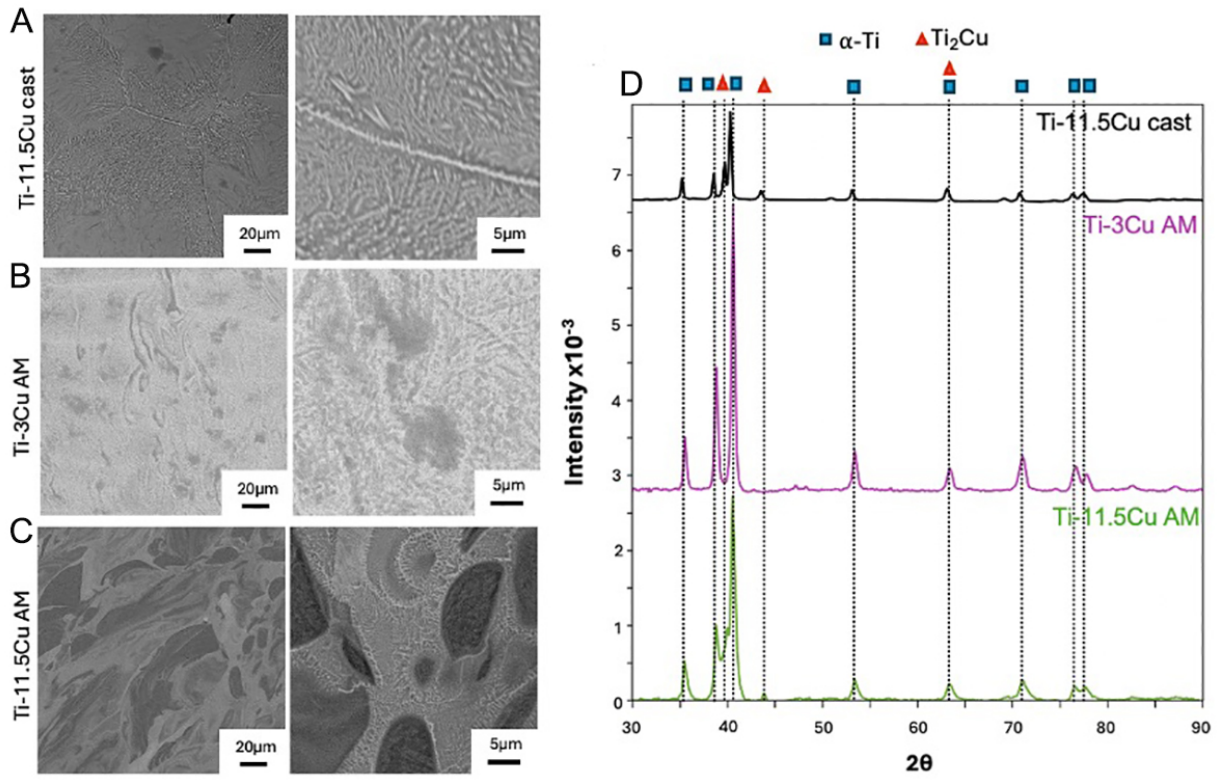


Figure 4. Low and high magnification BSE SEM images of (A) Ti-11.5Cu cast and BP-LPBF, (B) Ti-3Cu, and (C) Ti-11.5Cu. (D) XRD spectra show the presence of Ti and Ti_2Cu. All micrographs are presented in the build orientation, with the build direction (BD) oriented vertically upwards, This figure is reprinted with permission[21].

Microstructural characterisation and phase identification

Figure 4 presents backscattered electron micrographs of cast Ti-11.5Cu (extracted from[20]), as well as BP-LPBF samples with 3 and 11.5 wt.% Cu at low and high magnification. Rabbitt *et al.* reported no antimicrobial efficacy in as cast Ti-11.5Cu alloys, on this basis, no cast Ti-3Cu samples were analysed[20]. As shown in Figure 4A, the Ti-11.5Cu cast exhibits a fine laminar structure, comprising of a mixture of acicular and equiaxed features. In contrast, Figure 4B demonstrates the Ti-3Cu BP-LPBF alloy displays a comparatively homogeneous structure, characterised by the overlapping, semi-elliptical melt pool features characteristic of LPBF processing. At high magnification, a fine microstructure is observed, likely consisting of an α-Ti matrix with finely dispersed nanoscale Ti_xCu precipitates. Whereas Figure 4C shows that the BP-LPBF Ti-11.5Cu alloy is much more heterogeneous, indicating phase segregation and increased formation of a secondary phase. There is a nanoscale lamellar-like microstructure of a Cu-rich phase, indicated to be Ti_2Cu by the XRD spectrum, not present in the LPBF Ti-3Cu alloy, shown in Figure 4D.

Spatial heterogeneity in the Ti-3Cu AM and Ti-11.5Cu AM microstructures was quantified using local standard deviation (σ) mapping of greyscale SEM images [Figure 5]. The heterogeneity maps [Figure 5A and B] reveal clear differences in both the magnitude and spatial distribution of intensity variations between the two compositions. Ti-3Cu AM exhibits a relatively uniform heterogeneity field, with low and evenly distributed σ values across the microstructure. In contrast, Ti-11.5Cu AM displays pronounced regions of elevated σ, forming interconnected networks that spatially correlate with visible phase boundaries and microstructural features in the SEM image. This indicates increased local contrast variation and more distinct phase separation at higher Cu content.

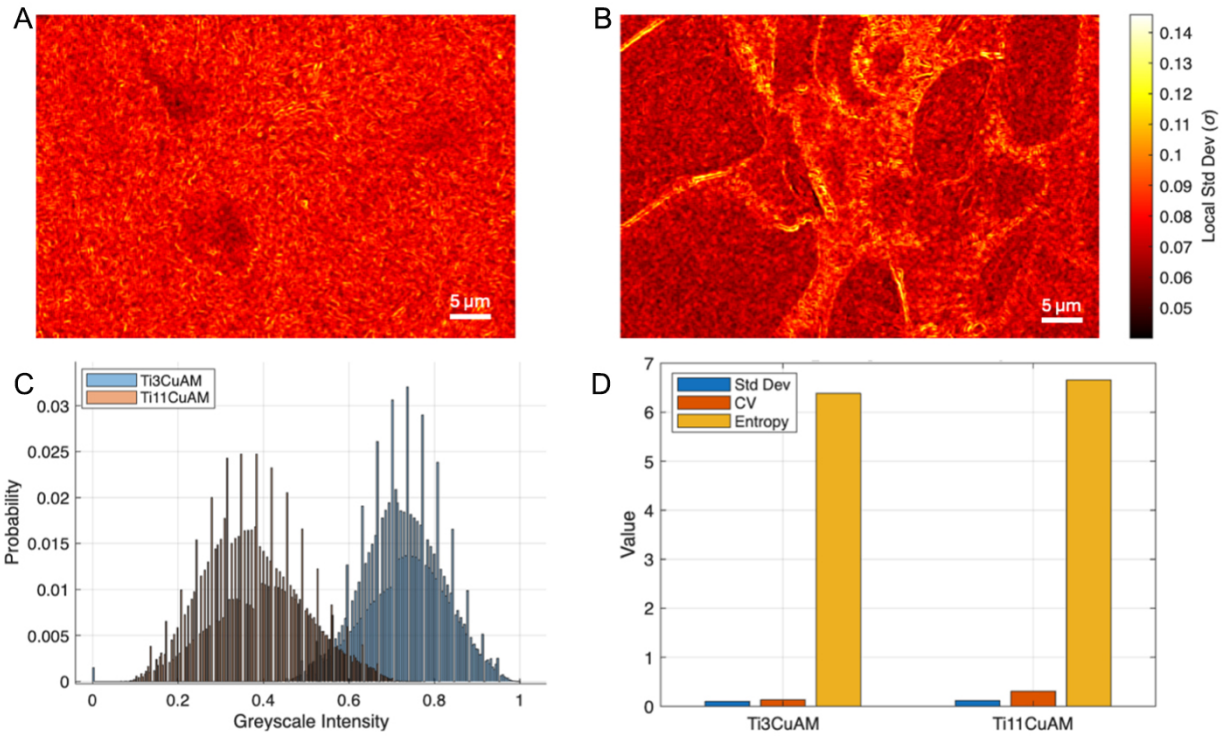


Figure 5. Spatial heterogeneity analysis of Ti-3Cu AM and Ti-11.5Cu AM microstructures. (A and B) Backscattered electron SEM images with overlaid corresponding local standard deviation (σ) maps calculated using a 15 × 15 pixel moving window, highlighting spatial variations in greyscale intensity. (C) Greyscale intensity distributions. (D) Quantitative heterogeneity metrics, including standard deviation, coefficient of variation (CV), and entropy.

The distribution of greyscale intensities [Figure 5C] further supports these observations. Ti-3Cu AM shows a narrower, unimodal distribution centred at higher greyscale values, consistent with a more homogeneous microstructure. Conversely, Ti-11.5Cu AM exhibits a broader distribution shifted towards lower intensities, with an extended tail, indicating a wider range of local environments and increased microstructural variability. Quantitative heterogeneity metrics [Figure 5D] reinforce these trends. While both samples show comparable absolute standard deviation values, Ti-11.5Cu AM exhibits a substantially higher coefficient of variation, reflecting greater relative heterogeneity when normalised by mean intensity. Additionally, the entropy is higher for Ti-11.5Cu AM, indicating increased complexity and disorder in the intensity distribution. Overall, these results demonstrate that increasing Cu content from 3 to 11.5 wt.% leads to a more heterogeneous and spatially complex microstructure, characterised by enhanced phase contrast and the development of localized high-variance regions associated with microstructural features.

Ti and Cu ion release

The antimicrobial efficacy of Ti-Cu alloys is closely related to their corrosion behaviour, where Cu ions and reactive oxygen species generated in a corrosion process exhibit antimicrobial effects[58-62]. However, the alloy must also maintain high overall corrosion resistance to remain biocompatible, making this a challenging balance to achieve. Figure 6 shows the release of Ti and Cu (as ions and neutral aqueous species) after 24 h into two environments: benign PBS (pH 7.3) and a harsher PBS containing 10 g/L BSA and 30 mM H_2O_2 (pH 7.3). The latter environment significantly enhances the corrosion of titanium alloys and simulates inflammatory conditions[53]. As expected, the amount of released Ti is significantly ($P < 0.01$) enhanced in PBS + BSA + H_2O_2 compared with PBS for all three investigated alloys [Figure 6A]. In contrast, Cu is released at higher amounts than Ti in the benign PBS [Figure 6B and C], consistent with the known behaviour of Cu-containing materials[63]. In the harshest solution, where the protective TiO_2 layer partially dissolved due to complex formation with H_2O_2[64], significantly more Ti than Cu is released ($P < 0.05$ for Ti-11.5Cu cast and Ti-3Cu AM, Figure 6D), with no discernible differences among the different alloys. Under a benign PBS

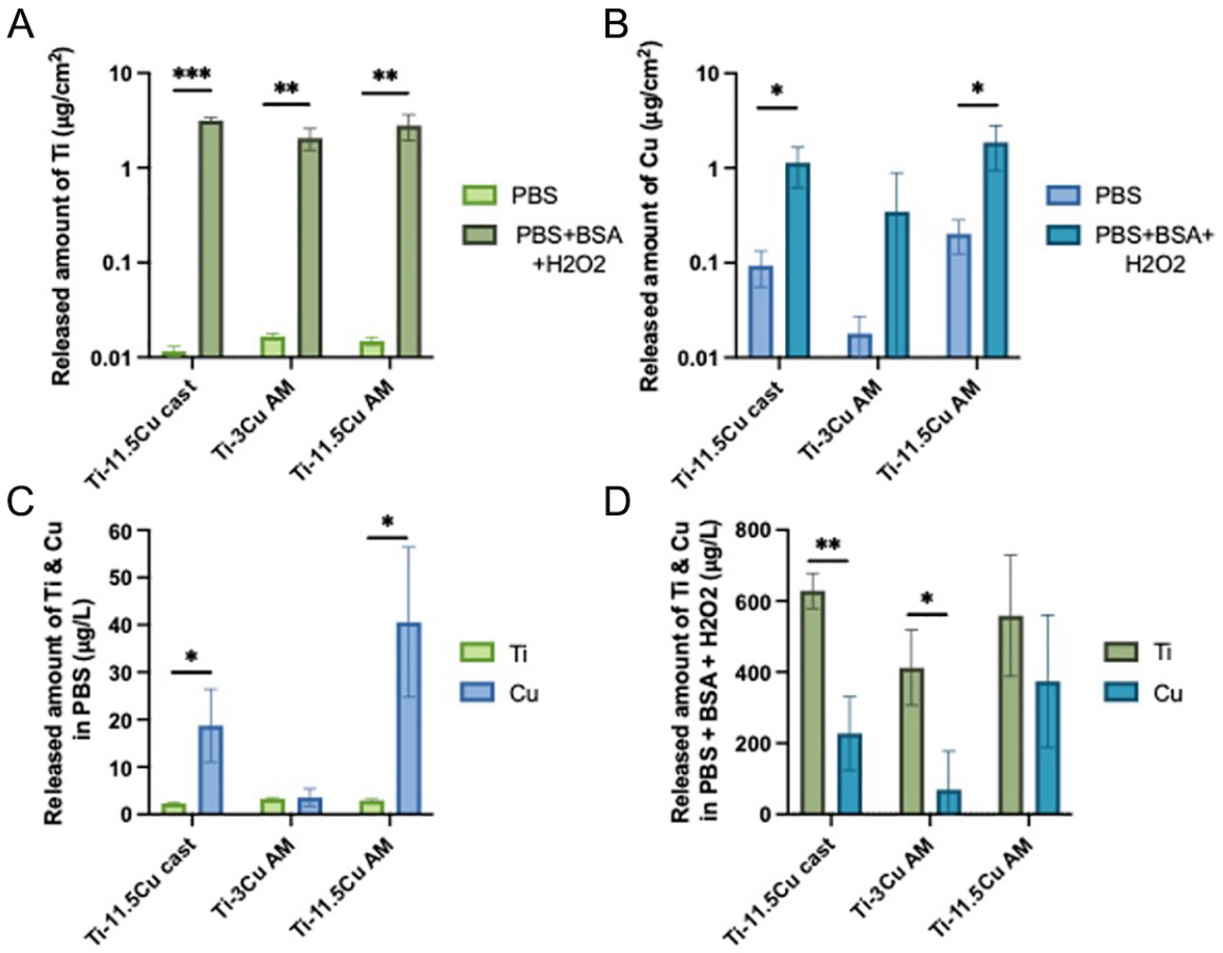


Figure 6. Released amount of Ti (A) and Cu (B) from as-cast Ti-11.5Cu, BP-LPBF Ti-3Cu, and Ti-11.5Cu alloys into PBS and PBS + 10 g/L BSA + 30 mM H_2O_2 after 24 h at 37 °C. The released amount (µg/cm²) is normalized to the solution volume and the exposed surface area and shown on a logarithmic scale because of the large difference between the two solutions. Corresponding aqueous concentrations (µg/L) of Ti and Cu in PBS (C) and PBS + 10 g/L BSA + 30 mM H_2O_2 (D). All shown values are blank- and dilution factor-corrected average values between triplicate samples, with the error bars representing the standard deviations. *$P < 0.05$; **$P < 0.01$; ***$P < 0.001$.

environment, however, clear differences emerge. Ti-3Cu AM releases the highest, although still very low, amount of Ti and the lowest amount of Cu among the three alloys ($P < 0.05$).

Contact angle

CA measurement is a key indicator of surface wettability, making it essential for understanding material interactions with fluids and biological cells, as well as inferring surface chemistry. Figure 7 shows the measured CA of water on the surface of (a) LPBF Ti64, (b) Ti-11.5Cu cast, (c) AM Ti-3Cu, and (d) AM Ti-11.5Cu. While all samples display hydrophilic behaviour, AM Ti-3Cu demonstrated a much lower CA value (59° ± 2°) than the Ti64 control (72° ± 2°) and Ti-11.5Cu cast (82° ± 4°) and AM (67° ± 2°). This suggests that variations in both composition and microstructure can significantly affect the hydrophobicity of AM Ti-Cu alloys.

Mechanical testing

Mechanical properties, summarised in Table 1, were evaluated using microhardness and tensile analysis [Figure 8]. Ti-11.5Cu cast and both AM Ti-3Cu and Ti-11.5Cu alloys exhibited similar microhardness values, with Ti-11.5Cu cast at 278 ± 20 HV0.1, Ti-3Cu AM at 287 ± 11 HV0.1 and Ti-11.5Cu AM at 283 ± 47 HV0.1,

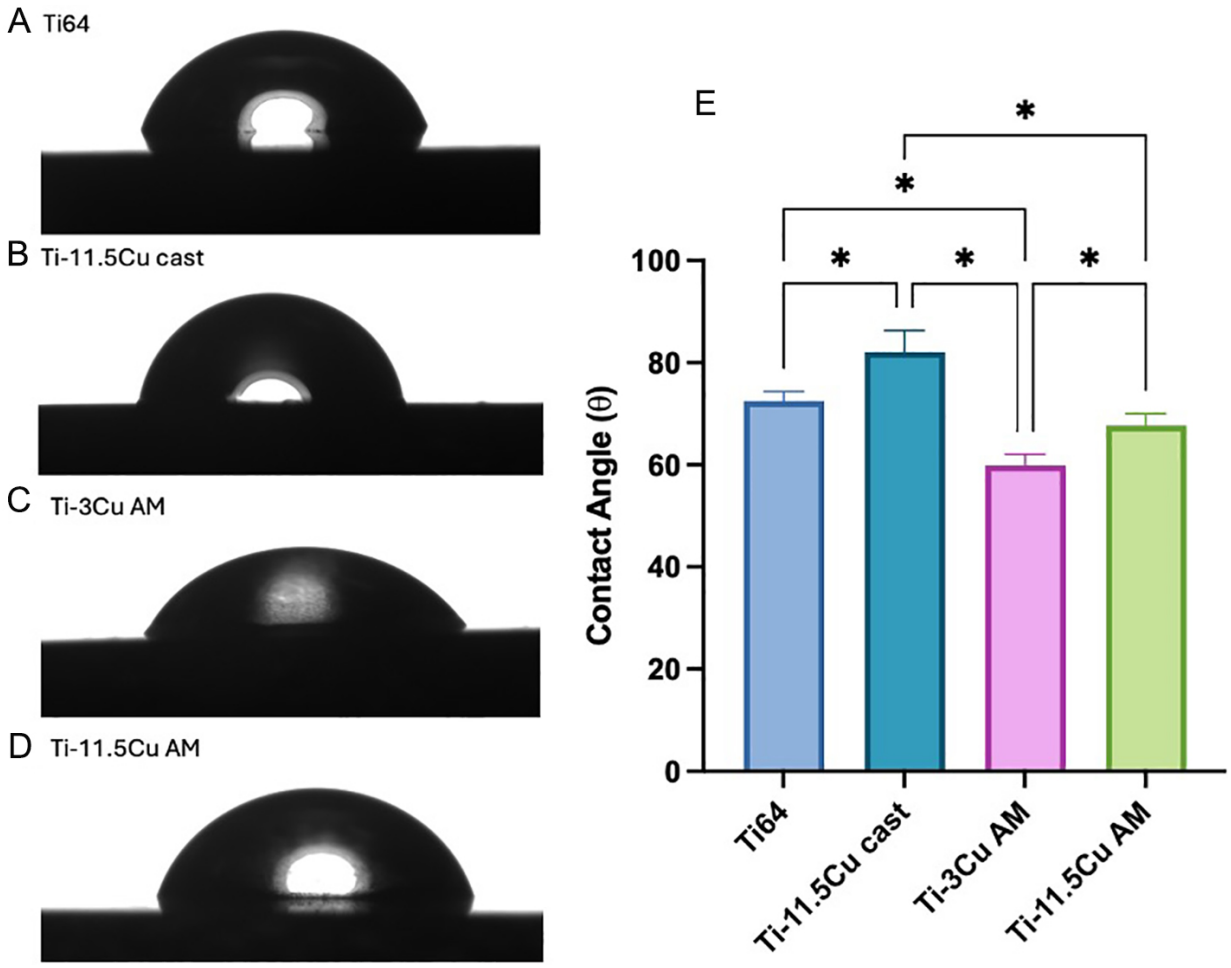


Figure 7. Images of water droplets on (A) Ti64, (B) Ti-11.5Cu as cast, (C) Ti-3Cu and (D) Ti-11.5Cu surfaces. With a summary of numerical data presented in (E) highlighting the significantly lower CA for Ti-3Cu compared with both the AM Ti-11.5Cu and as-cast sample and Ti-6Al-4V (n = 5), *P < 0.05. This figure is reprinted with permission[21].

though the latter showed increased variability between replicates. For the AM samples, the elastic modulus also decreased with increased copper content, from 62 ± 9 GPa for Ti-3Cu AM to 48 ± 3 GPa for Ti-11.5Cu AM. Most notably, tensile strength and ductility were significantly affected by the higher Cu content. Ti-3Cu AM exhibited a tensile strength of 939 ± 67 MPa and ductility of 12.6% ± 6.3%, whereas Ti-11.5Cu AM showed a reduction in both, with tensile strength falling to 248 ± 48 MPa and ductility to only 0.45% ± 0.1%. Unfortunately, due to the limited size of the as-cast specimens, it was not possible to carry out further mechanical testing beyond microhardness.

Antimicrobial analysis

Figure 9 compares the antimicrobial efficacy of the Ti-Cu alloys after 24 h of incubation with bacterial cultures, using Ti-6Al-4V and Cu as negative and positive controls, respectively, for (a) *S. aureus* and (b) *E. coli*. The Ti-6Al-4V control was defined as the baseline condition (0% antibacterial reduction), against which the antibacterial performance of the Ti-Cu alloys was normalised. These results demonstrate that enhanced antimicrobial effect is correlated to an increase in Cu concentration, apparent in both bacterial strains analysed. A bacterial reduction of 99.5% and 99.9% for AM Ti-3Cu and AM Ti-11.5Cu, respectively, was measured for *S. aureus* compared to the Ti-64 control, whereas against *E. coli* this increased to 99. 9% and 99.99%. Previous results suggest no antimicrobial efficacy for Ti-11.5Cu as cast specimens, as depicted in Figure 9, though some efficacy against *S. aureus* was achieved through heat treatments[20].

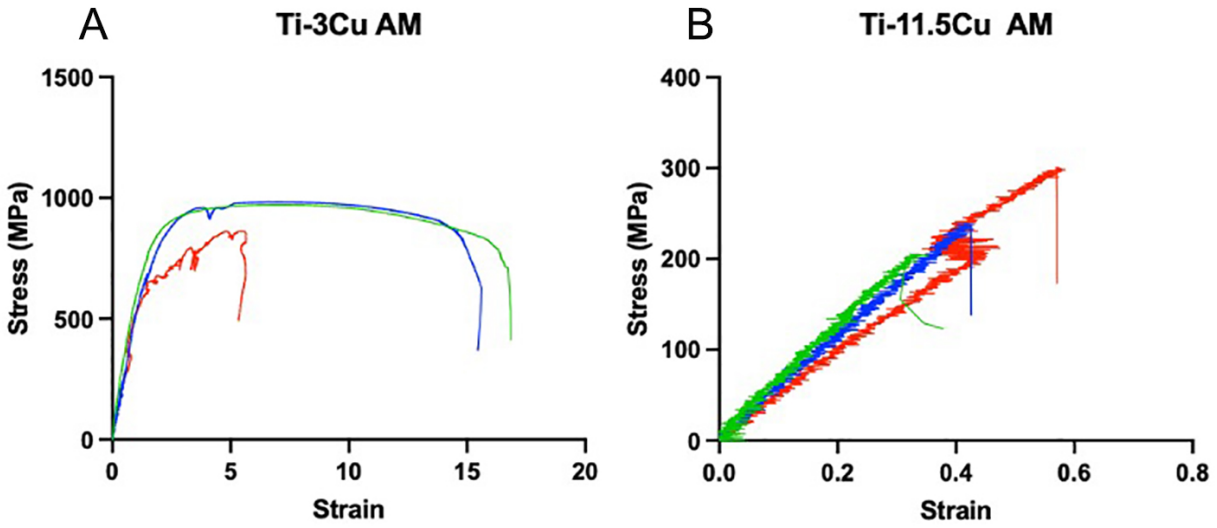


Figure 8. Stress-strain graphs for BP-LPBF (A) Ti-3Cu and (B) Ti-11.5Cu, with the three repeats represented in red, blue, and green.

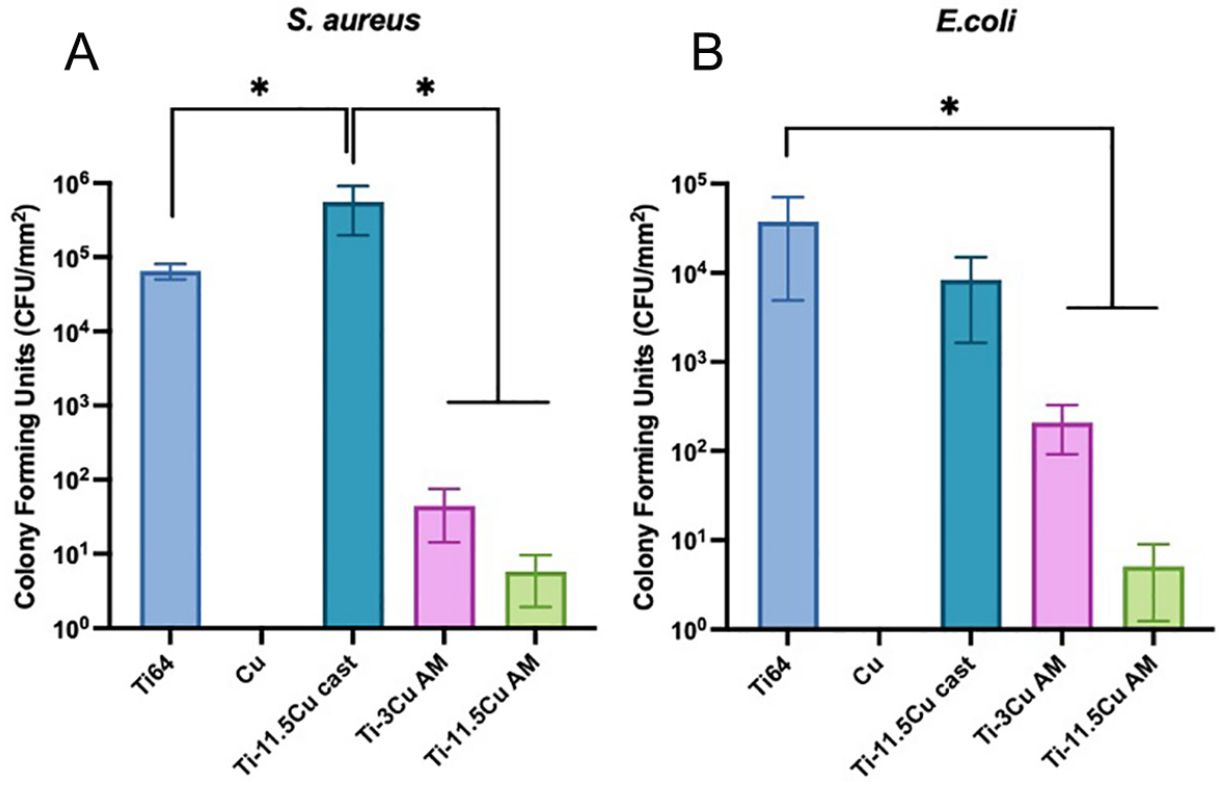


Figure 9. Antimicrobial analysis of Ti-Cu alloys relating to (A) *S. aureus* and (B) *E. coli* displaying the colony-forming units (CFU/mm²). *$P \leq 0.05$[21].

Table 1. Mechanical properties of the Ti-Cu alloys as measured through microhardness and tensile testing

Composition	Microhardness (HV0.1)	Elastic modulus (GPa)	Tensile strength (MPa)	Ductility (%)
Ti-11.5Cu cast	278 ± 20	-	-	-
Ti-3Cu AM	287 ± 11	62 ± 9	939 ± 67	12.6 ± 6.3
Ti-11.5Cu AM	283 ± 47	48 ± 3	248 ± 48	0.45 ± 0.1

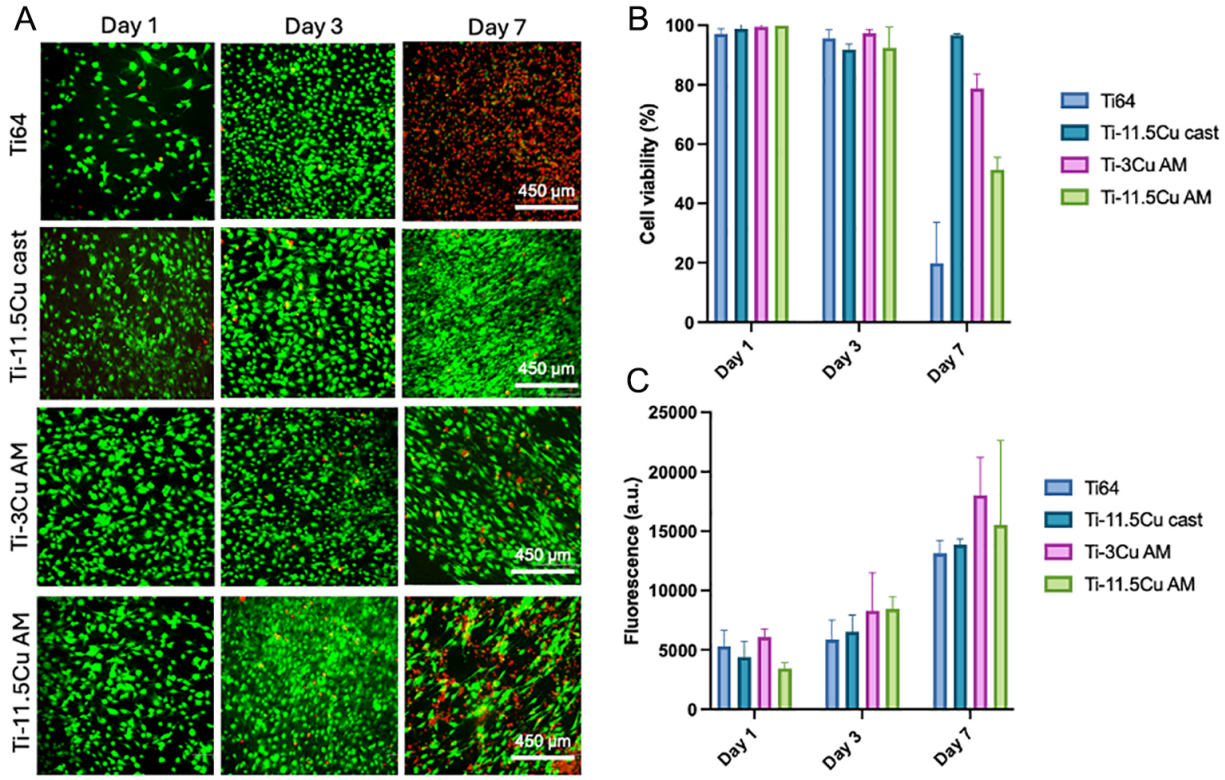


Figure 10. Influence of alloy composition and manufacturing method on murine pre-osteoblast cells over 7 days (A) fluorescent images of live (green) and dead (red) cells, (B) quantification of cell viability and (C) metabolic activity assessed via Alamar Blue assay[21].

Cytotoxicity

The cytotoxicity of the Ti-Cu alloys was assessed using live/dead staining and Alamar Blue assay [Figure 10] to evaluate the balance between antimicrobial activity and cytocompatibility. Minimal cell death was observed for all samples after 1 and 3 days. However, after 7 days, cell viability decreased to 78% and 51% for the LPBF Ti-3Cu and Ti-11.5Cu alloys, respectively, indicating increasing cytotoxicity with higher Cu content. This is to be compared to 96% and 20% for Ti-11.5Cu cast and Ti-6Al-4V alloy, respectively, Figure 10. For comparison, Ti-6Al-4V has known biocompatibility concerns due to the release of vanadium and aluminium ions. Although the severity of this toxicity remains under discussion in the literature, the static conditions commonly used in *in vitro* assays are likely to promote ion accumulation at the material surface and within cells[65-68]. This may exacerbate cytotoxic effects, as reflected in Figure 10.

DISCUSSION

This study demonstrates the utility of BP-LPBF AM as a platform for controlling manufacturing-induced microstructural heterogeneity, thereby governing antimicrobial, mechanical, and biological performance. By modulating Cu content and leveraging rapid solidification conditions inherent to LPBF, tailored phase distributions and microstructures were achieved, yielding distinct differences in antimicrobial efficacy and cytotoxicity compared to cast samples, as well as mechanical integrity.

Microstructural characterisation revealed that increasing the Cu content from 3 to 11.5 wt.% in the AM samples induced a transition from a largely homogenous α-Ti matrix to a heterogenous structure dominated by Ti_2Cu intermetallic phase formation. Ti-11.5Cu AM exhibited pronounced local intensity variation and high-σ regions corresponding to interconnected Cu-rich networks, whereas Ti-3Cu AM retained a more uniform distribution. Importantly, this heterogeneity is not solely composition-driven but is strongly

influenced by processing, as demonstrated by the narrower LPBF processing window observed for Ti-11.5Cu compared to Ti-3Cu. The lower energy density required for densification likely reduces melt pool mixing, promoting Cu segregation and reinforcing spatial heterogeneity. The differences observed between the LPBF and cast Ti-Cu alloys can be rationalised by the markedly different solidification conditions associated with each manufacturing route. During LPBF, cooling rates are typically several orders of magnitude higher than those encountered during conventional casting[29,69], resulting in substantial refinement of the α-Ti microstructure and the formation of elongated columnar prior β grains aligned with the build direction. In contrast, the cast Ti-11.5Cu alloy solidifies under near-equilibrium conditions, promoting coarser α-laths and larger equiaxed prior β grains. The resulting increase in grain boundary density and phase boundary area in LPBF alloys provides a greater number of energetically favourable sites for Cu segregation and Ti_2Cu precipitation.

In addition to grain refinement, rapid solidification strongly influences Ti_2Cu nucleation and growth behaviour. The LPBF process promotes solute trapping and local Cu enrichment within interdendritic regions, while repeated thermal cycling during subsequent layer deposition may further stimulate precipitation. Consequently, Ti_2Cu is expected to form as a finer and more spatially distributed intermetallic phase than in cast material, where slower cooling permits coarsening and reduced interfacial area. Such differences in precipitate morphology and connectivity are particularly relevant because α-Ti/Ti_2Cu interfaces are believed to act as local electrochemical couples. Therefore, the greater interfacial density and phase connectivity produced by LPBF may contribute to enhanced surface reactivity and antimicrobial performance. Furthermore, the steep thermal gradients inherent to LPBF generate significantly higher residual stress and defect densities than conventional casting, providing an additional source of microstructural heterogeneity that may influence corrosion and diffusion behaviour.

The ion release behaviour observed in this study provides critical insight into the relative contributions of ion-mediated and surface-mediated antimicrobial mechanisms in AM Ti-Cu alloys. While Cu ion release is widely reported as the primary antibacterial mechanism in Ti-Cu systems[70-72], the concentrations measured in this study are several orders of magnitude lower than reported minimum inhibitory concentrations (MICs), which are approximately 1,024 μg/mL for *S. aureus* and 480 μg/mL for *E. coli*[20,21], with bactericidal effects typically requiring concentrations in the range of hundreds to thousands of μg/mL[73-76]. In contrast, the Cu concentrations measured here are on the order of μg/L, corresponding to less than 0.01% of these bactericidal thresholds. While this comparison is indirect, it provides a strong upper bound on the possible contribution of bulk ion-mediated toxicity.

This disparity indicates that bulk Cu ion release alone cannot account for the observed antibacterial efficacy, particularly under physiological conditions, and therefore represents a minor contribution to the overall antimicrobial response. Instead, these findings point towards surface-mediated mechanisms as the dominant pathway. The pronounced spatial heterogeneity observed in Ti-11.5Cu AM provides a mechanistic basis for this behaviour. The formation of spatially distributed Cu-rich phases and interconnected Ti_2Cu networks introduces local electrochemical gradients and micro-galvanic interactions at the material surface. These features can generate elevated near-surface Cu activity and reactive sites that are not captured by bulk ICP measurements, enabling highly localised antibacterial interactions. Importantly, this distinction highlights that ICP-MS reflects cumulative dissolved Cu in the bulk medium rather than the transient, spatially confined Cu ion flux at the immediate biomaterial-bacteria interface, where antimicrobial activity is initiated and sustained. Furthermore, ICP-MS quantifies cumulative Cu release into the bulk solution and does not directly represent the local Cu ion flux at the biomaterial-bacteria interface, which governs antimicrobial activity. In addition, under physiological media such as PBS + BSA + H_2O_2, complexation and adsorption phenomena may further reduce the free Cu^{2+} fraction in solution, reinforcing the divergence between

measured total Cu release and biologically active Cu species.

Under these conditions, bacterial inactivation is therefore likely governed by direct surface contact and localised electrochemical disruption rather than uniform ion diffusion into the surrounding medium. Importantly, this mechanism is strongly dependent on the distribution and connectivity of Cu-rich phases, suggesting that microstructural heterogeneity may contribute to antimicrobial performance in addition to the effect of overall Cu content. However, the present study does not enable the independent effects of composition and microstructure to be separated. Under oxidative conditions, however, a secondary ion-mediated contribution becomes more significant. The presence of H_2O_2 and BSA promotes passive film breakdown and metal-protein complexation, resulting in increased Cu dissolution. In this regime, ion release may act synergistically with surface-mediated mechanisms, enhancing antibacterial efficacy. These findings therefore support a dual-mechanism model, in which ion release provides a conditional contribution, while surface-driven interactions dominate under physiological conditions. However, the present methodology does not enable direct decoupling of ion-mediated and surface-mediated contributions; therefore, the relative contributions of these mechanisms cannot be quantitatively resolved and are inferred based on indirect evidence. Furthermore, under physiological conditions, particularly inflammatory conditions, phase boundaries are highly susceptible to pitting. Thus, further analysis using electrochemical polarisation testing is required to assess the long-term *in vivo* safety.

In the present study, all Ti-Cu compositions demonstrated low overall ion release, well below these MIC thresholds, under physiological PBS conditions. These values indicate excellent passivation in neutral environments, consistent with the known biocompatibility and corrosion resistance of Ti-based alloys. However, exposure to oxidative conditions, designed to mimic inflammatory environments, dramatically accelerated both Ti and Cu dissolution across all compositions. The presence of H_2O_2 and BSA promotes breakdown of the passive oxide film and metal-protein complexation, thereby enhancing ion liberation[53].

These results suggest a dual antimicrobial paradigm in AM Ti-Cu alloys: under physiological conditions, surface-driven contact killing and micro-galvanic effects likely dominate, whereas in oxidative environments associated with infection or inflammation, enhanced Cu release may serve as an additional antimicrobial mechanism. This dynamic response may be advantageous for biomedical applications, where implants should remain biologically inert under healthy conditions yet responsive to infection-driven biochemical cues such as haematogenous seeding of infection onto a previously aseptic prosthesis, thought to occur in temporally late PJIs in at least 20% of *S. aureus* bacteraemia[77]. The increased spatial heterogeneity observed in Ti-11.5Cu AM may further contribute to this behaviour, as the presence of discrete Cu-rich regions and phase boundaries can enhance local electrochemical gradients and promote micro-galvanic interactions. These heterogeneities may facilitate localised ion release and reactive surface interactions, supporting contact-based antibacterial activity even in the absence of significant bulk ion release.

When compared to previous cast Ti-Cu alloys[20], AM-produced samples displayed superior antimicrobial performance, even at reduced Cu concentrations. It is assumed that Ti-6Al-4V does not exhibit intrinsic antimicrobial activity and is therefore treated as the baseline control material; however, a slight increase in CFU counts is observed for the cast Ti-11.5Cu sample (for *S. aureus*) compared to Ti-6Al-4V, suggesting that Ti-6Al-4V may also exhibit a modest antimicrobial effect. Despite comparable Cu content and the presence of Ti_2Cu phases, cast alloys do not exhibit equivalent antibacterial performance, highlighting that phase presence alone is insufficient without appropriate spatial distribution. This may be due to enhanced surface contact mechanisms and finer grain size imparted by AM, which can accelerate localised electrochemical activity and Cu release under certain conditions. However, as shown in Figure 6, Ti dissolution does not increase appreciably across the alloys in harsher solutions, raising questions regarding

the extent of galvanic corrosion. Notably, literature indicates that galvanic coupling in Ti-Cu systems may preferentially drive Cu dissolution rather than Ti[4,78,79], which aligns with the observed behaviour and supports the interpretation that galvanic corrosion is indeed operative in these alloys. Furthermore, the AM Ti-Cu alloys displayed cytocompatibility levels (Ti-3Cu: 78% and Ti-11.5Cu: 51% after 7 days) that reflect a trade-off with their superior antimicrobial efficacy, as these values were lower than those of the cast Ti-11.5Cu alloy (96% after 7 days). BP-LPBF Ti-3Cu, in particular, showed higher cell viability and reduced cytotoxicity over 7 days, likely due to its lower tendency for ion release and refined microstructure.

The comparison of AM and conventional approaches adds valuable context to the limited body of literature evaluating the impact of manufacturing method on antimicrobial performance. Due to the inconsistencies in antimicrobial test parameters across studies, ranging from bacterial strains and inoculum concentrations to incubation times and assay techniques (as demonstrated in Table 2), direct comparison is often challenging. This study provides a controlled analysis of alloys produced by different manufacturing routes under standardised testing conditions, offering key insights into how microstructural control via AM can optimise both biological and mechanical properties. To contextualise these findings, Table 2 summarises key trends across the literature, highlighting the variability in reported mechanisms and testing conditions. Notably, few studies account for microstructural differences and heterogeneity, reinforcing the distinction of the present work.

In contrast to conventional processing routes, where phase formation is largely composition-driven, AM allows heterogeneity to be actively tuned through processing conditions, providing a pathway to optimise competing properties such as antimicrobial activity, cytocompatibility, and mechanical integrity. Similar behaviour has been observed in LPBF-processed alloys such as Ti-6Al-4V, where processing parameters influence microstructure and resulting mechanical properties[82,83]. More broadly, AM has enabled the development of tailored microstructures in advanced alloys, reinforcing its capability to control structure-property relationships beyond conventional methods[84,85].

AM Ti-3Cu exhibits a favourable combination of microhardness (287 HV), elastic modulus (62 GPa), and excellent ductility (12.6%), making it well-suited for load-bearing applications. Its high and consistent hardness ensures reliable wear resistance, while its significant ductility provides fracture toughness. In contrast, AM Ti-11.5Cu, despite having a slightly lower elastic modulus (48 GPa), which is closer to that of cortical bone (30 GPa[86]) and could theoretically reduce stress shielding, suffers from extremely low ductility (0.45%). This extreme brittleness not only limits its formability and mechanical reliability, but also raises serious concerns about failure *in vivo*. The similar microhardness values observed for AM Ti-3Cu and Ti-11.5Cu reflect the local resistance to plastic deformation governed primarily by the α-Ti matrix and the presence of Cu in solid solution and fine intermetallic distributions. In contrast, the tensile strength is more sensitive to the continuity and morphology of the brittle Ti_2Cu phase. At higher Cu contents (Ti-11.5Cu), the formation of a more continuous and interconnected Ti_2Cu network promotes early crack initiation and rapid crack propagation under tensile loading, significantly reducing load-bearing capacity despite only minor changes in local hardness.

The mechanical behaviour of the alloys is strongly governed by microstructural heterogeneity. While Ti-3Cu AM exhibits a favourable combination of hardness and ductility, Ti-11.5Cu AM shows severe embrittlement despite similar average hardness values. Spatial heterogeneity mapping reveals localised Cu-rich intermetallic networks in Ti-11.5Cu AM, which act as stress concentrators and crack initiation sites, explaining the reduction in ductility from 12.6% to 0.45%. This relationship is further supported by the increase in coefficient of variation from 0.129 to 0.304, indicating a substantial rise in heterogeneity. While this enhances antimicrobial performance, it simultaneously compromises mechanical integrity and cytocompatibility, demonstrating a clear heterogeneity-driven trade-off.

Table 2. Summary of Ti-Cu compositions analysed throughout literature in relation to the method of antimicrobial testing, bacteria and their manufacturing method

Alloy (Ti-(wt.%)Cu)	Manufacture method	Thermomechanical treatment conditions	Bacteria and contact time	Antimicrobial efficacy	Attributed mode of action	Reference
Ti-3Cu	Wrought bar + HT	Solid solution treated at 900 °C for 5 h, aged at 400 °C for 24 h	*S. aureus* for 24 h	99.99%	Nano-scale galvanic cell disrupting proton motive force and resisting ATP production	[1]
Ti-5Cu	Ball mill + hot pressure sintered	Hot pressure sintered under vacuum conditions at 30 MPa and 1,050 °C	*P. gingivalis* for 18 and 24 h	36% and 54%	Cu ion release	[8]
Ti-10Cu				69% and 75%		
Ti-1Cu	Arc melted + HT	900 °C for 18 h, then 798 °C for 24 h, salt-brine water quench	*S. epidermis* for 6 h	4%	Cu ion release	[7]
Ti-2.5Cu				13%		
Ti-3Cu				16%		
Ti-10Cu				27%		
Ti-2Cu	Ball mill + hot pressure sintered	5-35 MPa pressure at 850-1,080 °C for 30-60 min	*S. aureus* for 24 h	79%	Cu ion release	[4]
Ti-5Cu				99%		
Ti-10Cu				99.99%		
Ti-25Cu				99.99%		
Ti-2Cu			*E. coli* for 24 h	57%		
Ti-5Cu				99.20%		
Ti-10Cu				99.99%		
Ti-25Cu				99.99%		
Ti-3Cu	SPS	SPS at 1,050 and 1,200 °C	*P. gingivalis* for 72 h	57%	Cu ion release and ROS production	[59]
Ti-5Cu				70%		
Ti-3Cu			*S. mutans for* 72 h	63%		
Ti-5Cu				78%		
Ti-3.5Cu	DED	n/a	*S. algae* for 24 h	40%	Micro-galvanic corrosion and Cu ion release	[80]
Ti-6.5Cu				70%		
Ti-8.5Cu				99.20%		
Ti-2Cu	LPBF	n/a	*S. aureus* for 24 h	99.75%	Not stated	[81]
Ti-5Cu				99.99%		
Ti-8Cu				100%		
Ti-3Cu	BP-LPBF	n/a	*S. aureus* for 24 h	99.5%	Surface contact, micro-galvanic corrosion and Cu ion release (in certain bodily conditions)	[This work]
Ti-11.5Cu				99.9%		
Ti-3Cu			*E. coli* for 24 h	99.9%		
Ti-11.5Cu				99.99%		

BP-LPBF: Blended powder laser powder bed fusion; ATP: adenosine triphosphate; HT: heat treated; SPS: spark plasma sintered; DED: directed energy deposition.

However, concerns regarding the mechanical properties of high-Cu-content alloys may also arise from studies using blended powder metallurgy routes, which do not accurately represent the final alloy component. Overall, the mechanical limitations of high-Cu-content AM alloys highlight significant challenges for long-term clinical reliability. Stable mechanical fixation is known to reduce infection risk and promote better tissue integration[87,88]. Thus, Ti-3Cu's superior mechanical profile could indirectly support

enhanced biological outcomes by enhancing stability. Furthermore, evaluating the translation to atomised powders is a critical next step to understand the influence on microstructure and the resulting mechanical and biological performance of produced parts. Therefore, translating high-Cu content alloy development to atomised powders and optimised AM methods is essential to accurately assess their microstructural stability, mechanical performance and biological behaviour.

Despite these advantages, concern regarding the long-term biocompatibility of Cu-containing Ti alloys persists. While Cu is an essential trace element in the body[89], excessive amounts of Cu can cause cytotoxicity and present with various health concerns[90]. The optimal concentration of Cu in Ti alloys remains a subject of debate, as its biocompatibility is likely linked to corrosion-induced ion release[91]. Increased Cu ion release from Ti-Cu alloys may not only compromise long-term biocompatibility but also contribute to the emergence of antimicrobial resistance against copper[92]. This is because prolonged exposure to sub-lethal concentrations of Cu ions can exert selective pressure on microorganisms, enabling them to develop adaptive resistance mechanisms such as efflux pumps, metal-binding proteins, and biofilm enhancement[93-97]. Although the Ti-11.5Cu alloy exhibits stronger antimicrobial properties than Ti-3Cu, the latter's lower Cu ion release may be advantageous for preventing cytotoxic effects and mitigating the risk of antimicrobial resistance. The increased cytotoxicity observed in Ti-11.5Cu AM may also be influenced by its higher microstructural heterogeneity, leading to localised regions of elevated Cu activity at the material surface that may exceed biologically tolerable limits despite low bulk ion release. This underscores the need for a nuanced approach in designing antimicrobial alloys and materials, ensuring that their antimicrobial benefits do not come at the cost of long-term safety and biological compatibility.

Given its balanced mechanical properties and moderate copper content, Ti-3Cu emerges as a promising surface coating material in multi-material designs, particularly when applied to Ti-6Al-4V substrates [Figure 11]. This approach offers the potential to synergize the high mechanical strength, fatigue resistance, and clinical acceptance of Ti-6Al-4V with the inherent antimicrobial properties of Ti-Cu alloys. AM techniques enable the creation of metallurgically bonded Ti-3Cu surface layers on Ti64 implants, with the potential to form functionally graded structures that maintain bulk mechanical integrity while providing antimicrobial protection at the tissue interface, similar to those shown in Bartolomeu *et al.*[98].

Such hybrid designs may be especially advantageous for porous lattice structures, which are often used to enhance osseointegration through increased surface area and roughness, but also present a risk of greater bacterial colonisation[99]. Producing the lattice surface structure in an antimicrobial Ti-Cu alloy solely, and keeping an underlying Ti-6Al-4V component, potentially offers new functionality without compromising mechanical integrity. This may be especially applicable for porous devices where the patient is at increased risk of infection, for example revision surgery or orthopaedic oncology patients that are often immunosuppressed (e.g., collar devices used in limb salvage procedures, see Figure 11C).

Collectively, these results demonstrate that the antimicrobial performance of Ti-Cu alloys cannot be predicted by composition alone, but is strongly governed by manufacturing-induced microstructural heterogeneity. The integration of process parameter optimisation, microstructural characterisation, and biological evaluation in this study highlights BP-LPBF as a powerful platform for the rapid development of multifunctional alloys, enabling simultaneous control of densification, phase distribution, and functional performance. A limitation of the present study is that alloy composition and manufacturing route were not independently controlled. Consequently, while trends suggest contributions from both Cu concentration and LPBF-induced microstructural refinement, no definitive conclusions can be drawn regarding the dominant factor governing antibacterial efficacy. Future work should include cast and additively manufactured alloys of identical compositions, as well as systematic variation of LPBF processing parameters, to isolate these effects.

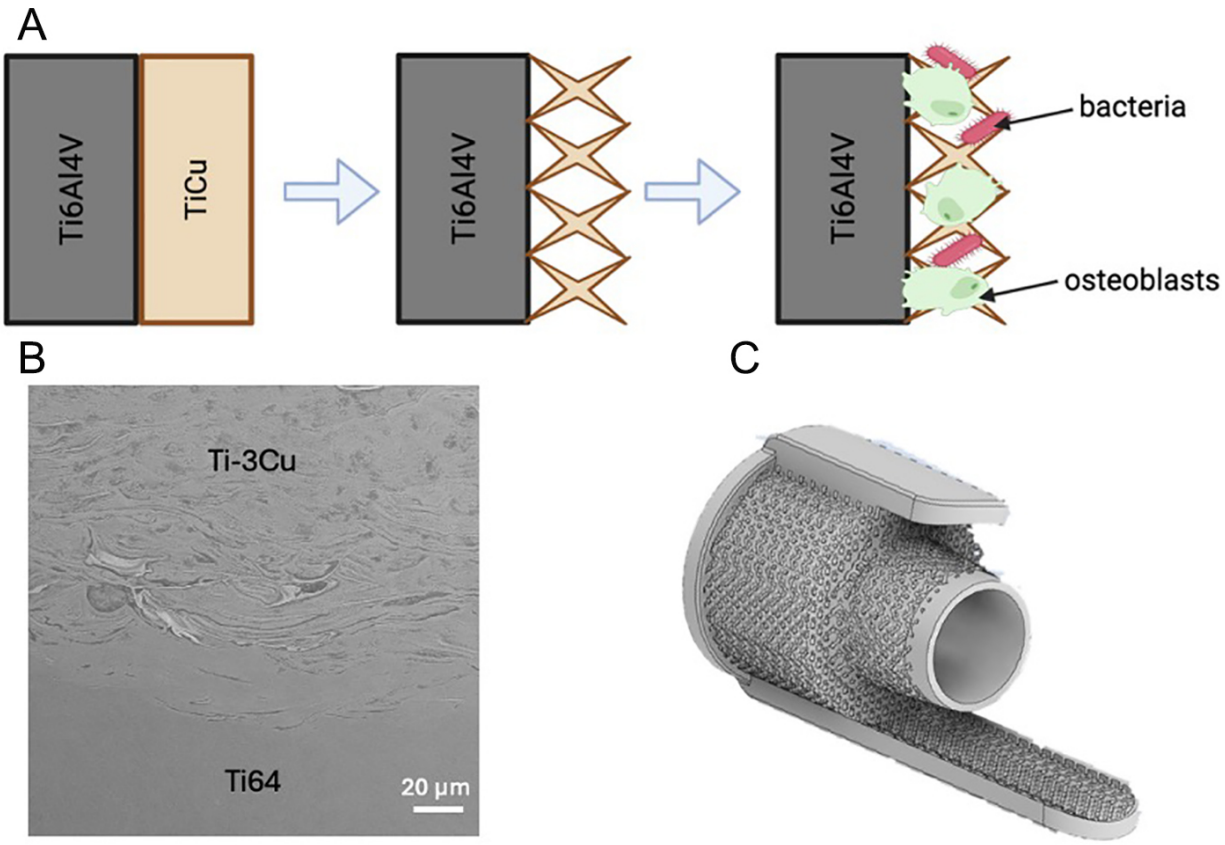


Figure 11. Concept and demonstration of a multi-material Ti-6Al-4V/Ti-Cu orthopaedic implant designed to integrate the mechanical reliability of Ti-6Al-4V with the antimicrobial and enhanced biological performance of Ti-Cu alloys. (A) Schematic illustration of the manufacturing strategy: a Ti-6Al-4V core is combined with a Ti-Cu region, enabling lattice or porous surface structures that support osteoblast attachment and osseointegration, while inhibiting bacterial colonization. Created in BioRender. Rabbitt, D. (2026) https://BioRender.com/hpldgqm. (B) Cross-sectional SEM micrograph of a bulk Ti-3Cu/Ti-6Al-4V multi-material interface with the build direction orientated vertically up, demonstrating metallurgical bonding and structural continuity between the two alloys. (C) CAD rendering of an orthopaedic oncology collar implant concept featuring a bulk structure and lattice surface to promote osseointegration.

CONCLUSION

This study highlights the transformative potential of BP-LPBF AM for controlling microstructural heterogeneity and, consequently, functional performance in next-generation biomedical alloys. Using Ti-Cu alloys as a case study, we demonstrate that antimicrobial behaviour is governed not by Cu content alone, but also the spatial distribution and connectivity of Cu-rich phases introduced during AM processing. Compared to cast equivalents, BP-LPBF produces heterogeneous microstructures with enhanced elemental segregation and surface reactivity, enabling superior antibacterial performance even at lower Cu contents.

Crucially, the measured Cu ion release was several orders of magnitude below bactericidal thresholds, strongly suggesting that antimicrobial activity is dominated by surface-mediated mechanisms, including micro-galvanic interactions and localised electrochemical disruption. Under oxidative conditions, increased ion release provides a secondary contribution, supporting a dual-mechanism model governed by microstructural design.

AM Ti-3Cu emerged as the most balanced composition, combining strong antibacterial activity with high cytocompatibility (78% cell viability at 7 days) and favourable mechanical properties (≈287 HV, 62 GPa

modulus, 12.6% ductility). In contrast, AM Ti-11.5Cu, despite achieving up to 99.99% bacterial reduction and possessing a lower elastic modulus (≈48 GPa), exhibited severe brittleness (0.45% ductility) and greater cytotoxicity (≈51% viability), linked to extensive Ti_2Cu formation, the highest Cu release, and microstructural inhomogeneity. These findings underscore the need to balance antimicrobial potency with mechanical reliability and biocompatibility, particularly given the risk of Cu-induced cytotoxicity or the development of resistance under chronic exposure.

More broadly, the work reinforces the critical influence of manufacturing route on alloy function: AM Ti-Cu outperformed cast counterparts despite lower Cu content, illustrating how microstructural refinement and surface reactivity inherent to LPBF can unlock superior biofunctionality. Collectively, this study establishes BP-LPBF as a powerful tool for rapid screening and optimisation of biofunctional alloys, and highlights the promise of AM Ti-3Cu for load-bearing implant applications and future functionally graded Ti-6Al-4V/Ti-Cu implant systems that combine mechanical stability with local antimicrobial protection.

Future work should focus on high-resolution microstructural characterisation, such as transmission electron microscopy (TEM) and Energy-dispersive X-ray spectroscopy (EDX), to further elucidate phase distribution, nanoscale segregation, and interfacial chemistry within Ti-Cu systems. In parallel, expanded biological evaluation is required to more precisely define the mechanisms of antibacterial action, including the relative roles of ion release, contact killing, and electrochemical interactions. At present, there is no established methodology to quantitatively decouple these contributions in AM alloys. The development of such approaches will be critical for advancing the rational design of antimicrobial biomaterials and fully exploiting the capability of AM to engineer mechanism-specific functionality.

DECLARATIONS

Acknowledgements

This work is based in part on the first author's doctoral dissertation submitted to the University of Birmingham and has been substantially expanded with additional experiments and analyses. Dr. Jonas Hedberg, Surface Science Western, is acknowledged for the maintenance of the ICP-MS instrument. Mr. Ivan Barker, Surface Science Western, is acknowledged for the training on the SEM instrument. The graphical abstract was created with BioRender.com (Created in BioRender. Rabbitt, D. (2026) https://BioRender.com/rnryvsk).

Authors' contributions

Formal analysis, investigation, methodology, writing - original draft, writing - review & editing: Rabbitt, D.
Formal analysis, investigation, methodology, writing - review & editing: Couling, K.; Guan, L.; Pütz, R. D.; Nikpour, S.
Formal analysis, methodology, writing - review & editing: Villapún, V. M.
Writing - review & editing: Carter, L. N.; Gibbons, G.; Hague, R.; Stevenson, J.
Funding acquisition, supervision, writing - review & editing: Hedberg, Y.; Knowles, A. J.; Cox, S. C.

Availability of data and materials

The data supporting the findings of this study are available from the corresponding author upon reasonable request.

AI and AI-assisted tools statement

Not applicable.

Financial support and sponsorship

Cox, S. C. acknowledges a UKRI Future Leaders Fellowship renewal (APP60831: Refine and Translate Bioinspired Alloys). Knowles, A. J. gratefully acknowledges funding from UKRI Future Leaders Fellowship MR/T019174/1 & MR/Y034155/1, and Royal Academy of Engineering Research Fellowship RF\201819\18\158. Canada Research Chairs Program (grant numbers CRC-2019-00425, CRC-2024-00200,

recipient Hedberg, Y.), Ontario Research Fund (Early Researcher Award, ER22-17-268, recipient Hedberg, Y.; Small Infrastructure Fund, grant number 42507, recipient Hedberg, Y.), Western University (start-up funds, recipient Hedberg, Y.), Canada Foundation for Innovation (John R. Evans Leaders Fund, grant number 42507, recipient Hedberg, Y.), and Natural Sciences and Engineering Research Council of Canada (Discovery Grants, RGPIN-2021-03997, recipient Hedberg, Y.).

Conflicts of interest

All authors declared that there are no conflicts of interest.

Ethical approval and consent to participate

Not applicable.

Consent for publication

Not applicable.

Copyright

© The Author(s) 2026.

REFERENCES

1. Zhang, Z.; Zheng, G.; Li, H.; et al. Anti-bacterium influenced corrosion effect of antibacterial Ti-3Cu alloy in Staphylococcus aureus suspension for biomedical application. *Mater. Sci. Eng. C.* **2019**, *94*, 376-84. DOI
2. Korda, A. A.; Munawaroh, S.; Basuki, E. A. The antimicrobial activity and characterization of the cast titanium copper alloys with variations of copper content. *IOP. Conf. Ser. Mater. Sci. Eng.* **2019**, *547*, 012002. DOI
3. Zhang, E.; Li, F.; Wang, H.; et al. A new antibacterial titanium-copper sintered alloy: preparation and antibacterial property. *Mater. Sci. Eng. C.* **2013**, *33*, 4280-7. DOI
4. Liu, J.; Li, F.; Liu, C.; et al. Effect of Cu content on the antibacterial activity of titanium-copper sintered alloys. *Mater. Sci. Eng. C.* **2014**, *35*, 392-400. DOI
5. Liu, R.; Memarzadeh, K.; Chang, B.; et al. Antibacterial effect of copper-bearing titanium alloy (Ti-Cu) against streptococcus mutans and porphyromonas gingivalis. *Sci. Rep.* **2016**, *6*, 29985. DOI PubMed PMC
6. Liu, R.; Tang, Y.; Zeng, L.; et al. In vitro and in vivo studies of anti-bacterial copper-bearing titanium alloy for dental application. *Dent. Mater.* **2018**, *34*, 1112-26. DOI
7. Fowler, L.; Janson, O.; Engqvist, H.; Norgren, S.; Öhman-Mägi, C. Antibacterial investigation of titanium-copper alloys using luminescent Staphylococcus epidermidis in a direct contact test. *Mater. Sci. Eng. C.* **2019**, *97*, 707-14. DOI
8. Bai, B.; Zhang, E.; Liu, J.; Zhu, J. The anti-bacterial activity of titanium-copper sintered alloy against *Porphyromonas gingivalis in vitro*. *Dent. Mater. J.* **2016**, *35*, 659-67. DOI PubMed
9. Simonelli, M.; Aboulkhair, N. T.; Cohen, P.; et al. A comparison of Ti-6Al-4V in-situ alloying in selective laser melting using simply-mixed and satellited powder blend feedstocks. *Mater. Charact.* **2018**, *143*, 118-26. DOI
10. Ma, M.; Zhao, M.; Ji, R.; Guo, Y.; Li, D.; Zeng, S. Adjusting the dose of ag-ion implantation on TiN-Ag-modified SLA-Ti creates different micronanostructures: implications on bacteriostasis, biocompatibility, and osteogenesis in dental implants. *ACS. Omega.* **2023**, *8*, 39269-78. DOI PubMed PMC
11. Luo, S.; Paisansuthichol, S.; Tran, N.; Qian, M.; Song, T. Biomedical titanium-tantalum alloys for orthopedic implant applications: From manufacturing to biological performance. *Bioact. Mater.* **2026**, *61*, 830-78. DOI PubMed PMC
12. Mitra, I.; Bose, S.; Dernell, W. S.; et al. 3D Printing in alloy design to improve biocompatibility in metallic implants. *Mater. Today.* **2021**, *45*, 20-34. DOI PubMed PMC
13. Fu, S.; Zhang, Y.; Qin, G.; Zhang, E. Antibacterial effect of Ti Ag alloy motivated by Ag-containing phases. *Mater. Sci. Eng. C.* **2021**, *128*, 112266. DOI
14. Mosallanejad, M.; Niroumand, B.; Aversa, A.; Manfredi, D.; Saboori, A. Laser powder bed fusion in-situ alloying of Ti-5%Cu alloy: process-structure relationships. *J. Alloys. Compd.* **2021**, *857*, 157558. DOI
15. Soro, N.; Attar, H.; Brodie, E.; Veidt, M.; Molotnikov, A.; Dargusch, M. S. Evaluation of the mechanical compatibility of additively manufactured porous Ti-25Ta alloy for load-bearing implant applications. *J. Mech. Behav. Biomed. Mater.* **2019**, *97*, 149-58. DOI PubMed
16. Fischer, M.; Joguet, D.; Robin, G.; Peltier, L.; Laheurte, P. In situ elaboration of a binary Ti-26Nb alloy by selective laser melting of elemental titanium and niobium mixed powders. *Mater. Sci. Eng. C.* **2016**, *62*, 852-9. DOI

17. Polozov, I.; Sufiiarov, V.; Popovich, A.; Masaylo, D.; Grigoriev, A. Synthesis of Ti-5Al, Ti-6Al-7Nb, and Ti-22Al-25Nb alloys from elemental powders using powder-bed fusion additive manufacturing. *J. Alloys. Compd.* **2018**, *763*, 436-45. DOI
18. Kang, N.; Li, Y.; Lin, X.; Feng, E.; Huang, W. Microstructure and tensile properties of Ti-Mo alloys manufactured via using laser powder bed fusion. *J. Alloys. Compd.* **2019**, *771*, 877-84. DOI
19. Grigoriev, A.; Polozov, I.; Sufiiarov, V.; Popovich, A. In-situ synthesis of Ti_2AlNb-based intermetallic alloy by selective laser melting. *J. Alloys. Compd.* **2017**, *704*, 434-42. DOI
20. Rabbitt, D.; O'kelly, P.; Villapún, V. M.; Carter, L. N.; Knowles, A. J.; Cox, S. C. Antimicrobial titanium-copper alloys: the role of microstructure in arc-melted compositions. *Adv. Eng. Mater.* **2025**, *27*, 2500347. DOI
21. Rabbitt, D. L. A. Development of antimicrobial metal alloys. University of Birmingham; 2025. Available from: https://etheses.bham.ac.uk/id/eprint/16231/ [Last accessed on 21 Aug 2026].
22. Rabbitt, D.; Villapún, V. M.; Carter, L. N.; et al. Rethinking biomedical titanium alloy design: a review of challenges from biological and manufacturing perspectives. *Adv. Healthc. Mater.* **2024**, *14*, 2403129. DOI PubMed PMC
23. Zhang, L. C.; Chen, L. Y. A review on biomedical titanium alloys: recent progress and prospect. *Adv. Eng. Mater.* **2019**, *21*, 1801215. DOI
24. Wu, C.; Lin, P.; Huang, S.; et al. Revisiting alloy design of low-modulus biomedical β-Ti alloys using an artificial neural network. *Materialia* **2022**, *21*, 101313. DOI
25. Stráský, J.; Harcuba, P.; Václavová, K.; et al. Increasing strength of a biomedical Ti-Nb-Ta-Zr alloy by alloying with Fe, Si and O. *J. Mech. Behav. Biomed. Mater.* **2017**, *71*, 329-36. DOI
26. Scipioni Bertoli, U.; Guss, G.; Wu, S.; Matthews, M. J.; Schoenung, J. M. In-situ characterization of laser-powder interaction and cooling rates through high-speed imaging of powder bed fusion additive manufacturing. *Mater. Des.* **2017**, *135*, 385-96. DOI
27. Takata, N.; Liu, M.; Kodaira, H.; Suzuki, A.; Kobashi, M. Anomalous strengthening by supersaturated solid solutions of selectively laser melted Al-Si-based alloys. *Addit. Manuf.* **2020**, *33*, 101152. DOI
28. Farshidianfar, M. H.; Khajepour, A.; Gerlich, A. Real-time control of microstructure in laser additive manufacturing. *Int. J. Adv. Manuf. Technol.* **2015**, *82*, 1173-86. DOI
29. Thampy, V.; Fong, A. Y.; Calta, N. P.; et al. Subsurface cooling rates and microstructural response during laser based metal additive manufacturing. *Sci. Rep.* **2020**, *10*, 1981. DOI PubMed PMC
30. Liu, Y.; Jiang, W.; Chen, Z.; Xu, Q.; Zhang, Z.; He, J. Optimization of processing parameters and microstructure evolution of $(TiB+La_2O_3)/Ti_6Al_4V$ manufactured by laser melting deposition. *J. Mater. Res. Technol.* **2023**, *24*, 8086-97. DOI
31. Zhou, J.; Li, H.; Yu, Y.; et al. Fabrication of functionally graded materials from a single material by selective evaporation in electron beam powder bed fusion. *Mater. Sci. Eng. A.* **2020**, *793*, 139827. DOI
32. Majumdar, J. D.; Pinkerton, A.; Liu, Z.; Manna, I.; Li, L. Microstructure characterisation and process optimization of laser assisted rapid fabrication of 316L stainless steel. *Appl. Surf. Sci.* **2005**, *247*, 320-7. DOI
33. Ghouse, S.; Babu, S.; Van Arkel, R. J.; Nai, K.; Hooper, P. A.; Jeffers, J. R. The influence of laser parameters and scanning strategies on the mechanical properties of a stochastic porous material. *Mater. Des.* **2017**, *131*, 498-508. DOI
34. Carter, L. N.; Martin, C.; Withers, P. J.; Attallah, M. M. The influence of the laser scan strategy on grain structure and cracking behaviour in SLM powder-bed fabricated nickel superalloy. *J. Alloys. Compd.* **2014**, *615*, 338-47. DOI
35. Ng, C.; Bermingham, M.; Dargusch, M. Controlling grain size, morphology and texture in additively manufactured β-titanium alloy with super transus hot isostatic pressing. *Addit. Manuf.* **2022**, *59*, 103176. DOI
36. Wang, Z.; Xiao, Z.; Tse, Y.; Huang, C.; Zhang, W. Optimization of processing parameters and establishment of a relationship between microstructure and mechanical properties of SLM titanium alloy. *Opt. Laser. Technol.* **2019**, *112*, 159-67. DOI
37. Hassanin, H.; El-sayed, M. A.; Ahmadein, M.; et al. Optimising surface roughness and density in titanium fabrication via laser powder bed fusion. *Micromachines* **2023**, *14*, 1642. DOI PubMed PMC
38. Li, Z.; Kucukkoc, I.; Zhang, D. Z.; Liu, F. Optimising the process parameters of selective laser melting for the fabrication of Ti_6Al_4V alloy. *Rapid. Prototyp. J.* **2018**, *24*, 150-9. DOI
39. Bocchetta, P.; Chen, L.; Tardelli, J. D. C.; Reis, A. C. D.; Almeraya-Calderón, F.; Leo, P. Passive layers and corrosion resistance of biomedical Ti-6Al-4V and β-Ti alloys. *Coatings* **2021**, *11*, 487. DOI
40. Rack, H.; Qazi, J. Titanium alloys for biomedical applications. *Mater. Sci. Eng. C.* **2006**, *26*, 1269-77. DOI
41. Mahmoudi, P.; Akbarpour, M. R.; Lakeh, H. B.; Jing, F.; Hadidi, M. R.; Akhavan, B. Antibacterial Ti-Cu implants: a critical review on mechanisms of action. *Mater. Today. Bio.* **2022**, *17*, 100447. DOI PubMed PMC
42. Tran, T. Q.; Chinnappan, A.; Lee, J. K. Y.; et al. 3D printing of highly pure copper. *Metals* **2019**, *9*, 756. DOI
43. Ngo, T. D.; Kashani, A.; Imbalzano, G.; Nguyen, K. T.; Hui, D. Additive manufacturing (3D printing): a review of materials, methods, applications and challenges. *Compos. Part. B. Eng.* **2018**, *143*, 172-96. DOI

44. Jiang, Q.; Zhang, P.; Yu, Z.; et al. A review on additive manufacturing of pure copper. *Coatings* **2021**, *11*, 740. DOI
45. Wang, J. C.; Li, Y. H.; Yuan, Y. J.; Liu, Y. J.; Zhang, L. C. Advances in laser powder bed fusion of copper and copper alloys: microstructure, mechanical behavior, and conductivity. *cMat* **2025**, *2*, e70021. DOI
46. Zhu, M.; Miao, J.; Zhou, X.; Zhang, E.; Liu, Z.; Yang, H. Corrosion resistance and antibacterial properties of Ti-3Cu alloy prepared by selective laser melting. *Trans. Nonferrous. Met. Soc. China.* **2025**, *35*, 143-56. DOI
47. Zhang, E.; Ren, J.; Li, S.; Yang, L.; Qin, G. Optimization of mechanical properties, biocorrosion properties and antibacterial properties of as-cast Ti-Cu alloys. *Biomed. Mater.* **2016**, *11*, 065001. DOI
48. Bao, M.; Liu, Y.; Wang, X.; et al. Optimization of mechanical properties, biocorrosion properties and antibacterial properties of wrought Ti-3Cu alloy by heat treatment. *Bioact. Mater.* **2018**, *3*, 28-38. DOI PubMed PMC
49. Ji, H.; Zhao, M.; Xie, B.; et al. Corrosion and antibacterial performance of novel selective-laser-melted (SLMed) Ti-xCu biomedical alloys. *J. Alloys. Compd.* **2021**, *864*, 158415. DOI
50. Tao, S.; Xu, J.; Yuan, L.; Luo, J.; Zheng, Y. Microstructure, mechanical properties and antibacterial properties of the microwave sintered porous Ti-3Cu alloys. *J. Alloys. Compd.* **2020**, *812*, 152142. DOI
51. Shannon, C. E. A mathematical theory of communication. *Bell. Syst. Tech. J.* **1948**, *27*, 379-423. DOI
52. Zhang, C.; Deng, Y.; Chong, M.; Zhang, Z.; Tan, Y. Entropy-based re-sampling method on SAR class imbalance target detection. *ISPRS. J. Photogramm. Remote. Sens.* **2024**, *209*, 432-47. DOI
53. Hedberg, Y. S.; Žnidaršič, M.; Herting, G.; Milošev, I.; Odnevall Wallinder, I. Mechanistic insight on the combined effect of albumin and hydrogen peroxide on surface oxide composition and extent of metal release from Ti_6Al_4V. *J. Biomed. Mater. Res.* **2018**, *107*, 858-67. DOI PubMed PMC
54. Gussev, M. N.; Busby, J. T.; Field, K. G.; Sokolov, M. A.; Gray, S. E. Role of scale factor during tensile testing of small specimens. In sixth international symposium on small specimen test techniques, ASTM International; 2014. DOI
55. Gupta, T. T.; Gupta, N. K.; Pestrak, M. J.; et al. Staphylococcus aureus aggregates on orthopedic materials under varying levels of shear stress. *Appl. Environ. Microbiol.* **2020**, *86*, e01234-20. DOI PubMed PMC
56. Viroxy. ISO 22196:2011. Available from: https://www.viroxylabs.com/microbiological-testing-services/disinfectant-efficacy-testing/iso-221962011/ [Last accessed on 14 Aug 2026].
57. Schneider, C. A.; Rasband, W. S.; Eliceiri, K. W. NIH image to ImageJ: 25 years of image analysis. *Nat. Methods.* **2012**, *9*, 671-5. DOI PubMed PMC
58. Zhang, E.; Wang, X.; Chen, M.; Hou, B. Effect of the existing form of Cu element on the mechanical properties, bio-corrosion and antibacterial properties of Ti-Cu alloys for biomedical application. *Mater. Sci. Eng. C.* **2016**, *69*, 1210-21. DOI
59. Yang, H. L.; Zou, L.; Juaim, A. N.; et al. Copper release and ROS in antibacterial activity of Ti-Cu alloys against implant-associated infection. *Rare. Metals.* **2023**, *42*, 2007-19. DOI
60. Mikolay, A.; Huggett, S.; Tikana, L.; Grass, G.; Braun, J.; Nies, D. H. Survival of bacteria on metallic copper surfaces in a hospital trial. *Appl. Microbiol. Biotechnol.* **2010**, *87*, 1875-9. DOI
61. Jeromen, A.; Nair, A.; Rodič, P.; et al. DED-LB manufactured Ti-6Al-4V-4Cu alloy: materials development, characterization, and in vivo biocompatibility. *J. Mater. Res. Technol.* **2025**, *39*, 5597-611. DOI
62. Hedberg, J.; Karlsson, H. L.; Hedberg, Y.; Blomberg, E.; Odnevall Wallinder, I. The importance of extracellular speciation and corrosion of copper nanoparticles on lung cell membrane integrity. *Colloid. Surface. B.* **2016**, *141*, 291-300. DOI PubMed
63. Midander, K.; Cronholm, P.; Karlsson, H. L.; et al. Surface characteristics, copper release, and toxicity of nano- and micrometer-sized copper and copper(II) oxide particles: a cross-disciplinary study. *Small* **2009**, *5*, 389-99. DOI
64. Tengvall, P.; Lundström, I.; Sjöqvist, L.; Elwing, H.; Bjursten, L. M. Titanium-hydrogen peroxide interaction: model studies of the influence of the inflammatory response on titanium implants. *Biomaterials* **1989**, *10*, 166-75. DOI PubMed
65. Thompson, G.; Puleo, D. Ti-6Al-4V ion solution inhibition of osteogenic cell phenotype as a function of differentiation timecourse in vitro. *Biomaterials* **1996**, *17*, 1949-54. DOI PubMed
66. Costa, B. C.; Tokuhara, C. K.; Rocha, L. A.; Oliveira, R. C.; Lisboa-Filho, P. N.; Costa Pessoa, J. Vanadium ionic species from degradation of Ti-6Al-4V metallic implants: in vitro cytotoxicity and speciation evaluation. *Mater. Sci. Eng. C.* **2019**, *96*, 730-9. DOI
67. Ghosh, S. K.; Saha, R.; Saha, B. Toxicity of inorganic vanadium compounds. *Res. Chem. Intermed.* **2014**, *41*, 4873-97. DOI
68. Hanawa, T. Metal ion release from metal implants. *Mater. Sci. Eng. C.* **2004**, *24*, 745-52. DOI
69. Kosiba, K.; Gustmann, T.; Kim, J. T.; et al. Experimental cooling rates during high-power laser powder bed fusion at varying processing conditions. *J. Alloys. Compd.* **2023**, *967*, 171773. DOI
70. Akbarpour, M. R.; Moniri Javadhesari, S. Densification and mechanical and antibacterial properties of low-cost powder metallurgy TiCu intermetallic alloy as a potential biomedical material. *JOM* **2020**, *72*, 3262-8. DOI
71. Li, Y. H.; Chen, N.; Cui, H. T.; Wang, F. Fabrication and characterization of porous Ti-10Cu alloy for biomedical application. *J. Alloys. Compd.* **2017**, *723*, 967-73. DOI

72. Korda, A. A.; Munawaroh, S.; Basuki, E. A. The antimicrobial activity and characterization of the cast titanium copper alloys with variations of copper content. *IOP. Conf. Ser. Mater. Sci. Eng.* **2019**, *547*, 012002. DOI
73. Crnčević, N.; El Sayed, A.; Hsino, M.; et al. Effect of copper salts on *Escherichia coli* and enterococcus faecalis biofilms in pipeline systems: implications for microbial control and hydraulic performance. *Appl. Sci.* **2025**, *15*, 8042. DOI
74. Reyes-Jara, A.; Cordero, N.; Aguirre, J.; Troncoso, M.; Figueroa, G. Antibacterial effect of copper on microorganisms isolated from bovine mastitis. *Front. Microbiol.* **2016**, *7*, 626. DOI PubMed PMC
75. Benhalima, L.; Amri, S.; Bensouilah, M.; Ouzrout, R. Antibacterial effect of copper sulfate against multi-drug resistant nosocomial pathogens isolated from clinical samples: effect of copper sulfate on clinical isolates. *Pak. J. Med. Sci.* **2019**, *35*, 1322-8. DOI PubMed PMC
76. Zevenhuizen, L. P. T. M.; Dolfing, J.; Eshuis, E. J.; Scholten-Koerselman, I. J. Inhibitory effects of copper on bacteria related to the free ion concentration. *Microb. Ecol.* **1979**, *5*, 139-46. DOI
77. Honkanen, M.; Jämsen, E.; Karppelin, M.; Huttunen, R.; Eskelinen, A.; Syrjänen, J. Periprosthetic joint infections as a consequence of bacteremia. *Open. Forum. Infect. Dis.* **2019**, *6*, ofz218. DOI PubMed PMC
78. Pina, V. G.; Amigó, V.; Muñoz, A. I. Microstructural, electrochemical and tribo-electrochemical characterisation of titanium-copper biomedical alloys. *Corros. Sci.* **2016**, *109*, 115-25. DOI
79. Luo, L.; Zhong, Q.; Chen, Z.; et al. 3D-printed copper-containing tailored titanium alloys with corrosion resistance, biocompatibility, and anti-inflammatory properties for enhanced guided bone regeneration. *Front. Bioeng. Biotechnol.* **2025**, *13*, 1647678. DOI PubMed PMC
80. Li, J.; Zhang, D.; Chen, X.; et al. Laser directed energy deposited, ultrafine-grained functional titanium-copper alloys tailored for marine environments: Antibacterial and anti-microbial corrosion studies. *J. Mater. Sci. Technol.* **2023**, *166*, 21-33. DOI
81. Liu, H.; Zhang, X.; Shi, L.; et al. Effect of Cu content on the properties of laser powder bed fused biomedical titanium alloys. *J. Mater. Res. Technol.* **2024**, *30*, 8992-8. DOI
82. Thijs, L.; Verhaeghe, F.; Craeghs, T.; Humbeeck, J. V.; Kruth, J. A study of the microstructural evolution during selective laser melting of Ti-6Al-4V. *Acta. Mater.* **2010**, *58*, 3303-12. DOI
83. Xu, W.; Brandt, M.; Sun, S.; et al. Additive manufacturing of strong and ductile Ti-6Al-4V by selective laser melting via in situ martensite decomposition. *Acta. Mater.* **2015**, *85*, 74-84. DOI
84. Kwabena Adomako, N.; Haghdadi, N.; Primig, S. Electron and laser-based additive manufacturing of Ni-based superalloys: a review of heterogeneities in microstructure and mechanical properties. *Mater. Des.* **2022**, *223*, 111245. DOI
85. Popovich, V.; Borisov, E.; Popovich, A.; Sufiiarov, V.; Masaylo, D.; Alzina, L. Functionally graded inconel 718 processed by additive manufacturing: crystallographic texture, anisotropy of microstructure and mechanical properties. *Mater. Des.* **2017**, *114*, 441-9. DOI
86. Chen, L.; Cui, Y.; Zhang, L. Recent Development in beta titanium alloys for biomedical applications. *Metals* **2020**, *10*, 1139. DOI
87. Schmidt, A. H.; Swiontkowski, M. F. Pathophysiology of infections after internal fixation of fractures. *J. Am. Acad. Orthop. Surg.* **2000**, *8*, 285-91. DOI PubMed
88. Foster, A. L.; Moriarty, T. F.; Zalavras, C.; et al. The influence of biomechanical stability on bone healing and fracture-related infection: the legacy of Stephan Perren. *Injury* **2021**, *52*, 43-52. DOI
89. Grass, G.; Rensing, C.; Solioz, M. Metallic copper as an antimicrobial surface. *Appl. Environ. Microbiol.* **2011**, *77*, 1541-7. DOI PubMed PMC
90. Gaetke, L. M.; Chow-Johnson, H. S.; Chow, C. K. Copper: toxicological relevance and mechanisms. *Arch. Toxicol.* **2014**, *88*, 1929-38. DOI PubMed PMC
91. Bandyopadhyay, A.; Mitra, I.; Ciliveri, S.; et al. Additively manufactured Ti-Ta-Cu alloys for the next-generation load-bearing implants. *Int. J. Extrem. Manuf.* **2023**, *6*, 015503. DOI PubMed PMC
92. Berg, J.; Thorsen, M. K.; Holm, P. E.; Jensen, J.; Nybroe, O.; Brandt, K. K. Cu exposure under field conditions coselects for antibiotic resistance as determined by a novel cultivation-independent bacterial community tolerance assay. *Environ. Sci. Technol.* **2010**, *44*, 8724-8. DOI PubMed
93. Gaurav, A.; Bakht, P.; Saini, M.; Pandey, S.; Pathania, R. Role of bacterial efflux pumps in antibiotic resistance, virulence, and strategies to discover novel efflux pump inhibitors. *Microbiology* **2023**, *169*, 001333. DOI PubMed PMC
94. Pietsch, F.; O'neill, A.; Ivask, A.; et al. Selection of resistance by antimicrobial coatings in the healthcare setting. *J. Hosp. Infect.* **2020**, *106*, 115-25. DOI
95. De Gaetano, G. V.; Lentini, G.; Famà, A.; Coppolino, F.; Beninati, C. Antimicrobial resistance: two-component regulatory systems and multidrug efflux pumps. *Antibiotics* **2023**, *12*, 965. DOI PubMed PMC
96. Boyd-Vorsah, S.; Torres, Ortiz. A.; Pulido, S.; Bui, B.; Yeh, P. J. Survival, resistance, and fitness dynamics of *Escherichia coli* populations after prolonged exposure to copper. *Evol. Med. Public. Health.* **2025**, *13*, 176-87. DOI PubMed PMC
97. Xu, Y.; Tan, L.; Li, Q.; Zheng, X.; Liu, W. Sublethal concentrations of heavy metals Cu^{2+} and Zn^{2+} can induce the emergence of bacterial multidrug resistance. *Environ. Technol. Innov.* **2022**, *27*, 102379. DOI

98. Bartolomeu, F.; Costa, M.; Alves, N.; Miranda, G.; Silva, F. Additive manufacturing of NiTi-Ti_6Al_4V multi-material cellular structures targeting orthopedic implants. *Opt. Lasers. Eng.* **2020**, *134*, 106208. DOI

99. Cox, S. C.; Jamshidi, P.; Eisenstein, N. M.; et al. Surface finish has a critical influence on biofilm formation and mammalian cell attachment to additively manufactured prosthetics. *ACS. Biomater. Sci. Eng.* **2017**, *3*, 1616-26. DOI

Disclaimer/Publisher's Note: All statements, opinions, and data contained in this publication are solely those of the individual author(s) and contributor(s) and do not necessarily reflect those of OAE and/or the editor(s). OAE and/or the editor(s) disclaim any responsibility for harm to persons or property resulting from the use of any ideas, methods, instructions, or products mentioned in the content.



© The Author(s) 2026. Open Access This article is licensed under a Creative Commons Attribution 4.0 International License (https://creativecommons.org/licenses/by/4.0/), which permits unrestricted use, sharing, adaptation, distribution and reproduction in any medium or format, for any purpose, even commercially, as long as you give appropriate credit to the original author(s) and the source, provide a link to the Creative Commons license, and indicate if changes were made.